Title: TET1 dioxygenase is required for FOXA2-associated chromatin remodeling in pancreatic beta-cell differentiation

Authors: Xinwei Wu[1#], Jianfang Li[2#], Minjung Lee[3], Qingping Lan[1], Jia Li[3], Yun Huang[3], De-Qiang Sun[2,3*], Ruiyu Xie[1*]

Affiliations:

[1] Centre of Reproduction, Development, and Aging, Faculty of Health Sciences, University of Macau, Taipa, Macau SAR.

[2] Department of Center Laboratory, The Fifth Affiliated Hospital of Guangzhou Medical University, Guangzhou 510700, China.

[3] Center for Epigenetics & Disease Prevention, Institute of Biosciences and Technology, College of Medicine, Texas A&M University, Houston, TX 77030, USA

# These authors contributed equally to the work.

* Correspondence: ruiyuxie@um.edu.mo; dsun@ibt.tamhsc.edu

Abstract: Existing knowledge of the role of epigenetic modifiers in pancreas development has exponentially increased. However, the function of TET dioxygenases in pancreatic endocrine specification remains obscure. We set out to tackle this issue using a human embryonic stem cell (hESC) differentiation system, in which *TET1*/*TET2*/*TET3* triple knock-out cells displayed severe defects in pancreatic β-cell specification. Integrative whole-genome analysis identified unique cell-type-specific hypermethylated regions (hyper-DMRs) displaying reduced chromatin activity and remarkable enrichment for the binding of FOXA2, a pioneer transcription factor essential for pancreatic endoderm specification. Intriguingly, hundreds of hyper-DMRs recently identified in type-2 diabetes pathogenesis overlapped with the hyper-DMRs we found in TET-deficient cells. Furthermore, transduction of *TET1* in *TET*-deficient cells effectively rescued β-cell differentiation and reversed hypermethylation and suppression of the β-cell determinant *PAX4*. Genome-wide mapping of TET1 showed that TET1 co-localized at a subset of FOXA2 targets featuring high levels of active chromatin modifications in pancreatic progenitors. Taking these findings together with the defective generation of functional β-cells upon TET1-inactivation, our study not only unveils an essential role of TET1-dependent epigenetic regulation in establishing β-cell identity but also provides a new mechanistic clue regarding the complex crosstalk between TET dioxygenases and pioneer transcription factors in lineage specification.

32 **Introduction**

33 During embryonic development, pluripotent human embryonic stem cells (hESCs) differentiate into
34 many diverse lineages that make up the complex tissues and organs of the human body. Pancreatic
35 lineage specification relies on cross-talk between the genome and environmental cues in the
36 progenitor niche. This cross-talk is mediated by cis-regulatory elements that play a prominent role in
37 spatiotemporal gene regulation during embryogenesis. In particular, distal regulatory elements, such
38 as enhancers, serve as information integration hubs that allow binding of multiple regulators,
39 including lineage-specific transcription factors (TFs) as well as epigenetic readers, writers, and
40 erasers to ensure integration of intrinsic and extrinsic environmental cues at these loci [1,2]. It was
41 recently demonstrated that pioneer TFs, such as FOXA1 and FOXA2, are required for proper
42 chromatin opening and establishment of enhancer marks H3K4me1 and H3K27ac during pancreatic
43 fate specification [3,4]. These pioneer TFs bind to nucleosomal DNA to initiate chromatin remodeling
44 associated with DNA demethylation at newly accessible enhancers [5-9].

45 DNA demethylation is mediated by ten-eleven-translocation methylcytosine dioxygenases
46 (TETs), which catalyze sequential oxidation of 5-methylcytosine (5mC) to 5-hydroxymethylcytosine
47 (5hmC), 5-formylcytosine, and 5-carboxylcytosine [10-14]. Distribution of 5hmC, a novel epigenetic
48 modification, is dynamically changed by and positively correlated with active gene transcription
49 during early lineage specification [15-17]. Consequently, inhibition of TET family enzymes (TET1,
50 TET2, and TET3) impairs cell fate commitment into neural, hematopoietic, cardiac, and several other
51 lineages [18-20]. Although TETs have been shown to regulate 5mC homeostasis during early embryonic

52 development, the functional relevance and mechanisms by which TETs regulate pancreatic endocrine
53 specification remain mostly unknown.

54 **Results**

55 **TET deficiency impairs pancreatic endoderm differentiation.** We previously demonstrated that
56 5hmC positively correlates with 'open' chromatin at poised and active enhancers in multiple
57 endodermal lineage intermediates using a stepwise hESC differentiation system toward pancreatic
58 progenitors [21]. To determine the biological significance of TET-dependent regulation during pancreas
59 specification, we generated *TET1*, *TET2*, and *TET3* single knock-out (KO), double knock-out (DKO),
60 and triple knock-out (TKO) H1 hESC lines using CRISPR/Cas9 technology (Supplementary Fig. 1a).
61 Mutations resulted in premature termination codons, which were confirmed by Sanger sequencing.
62 Global DNA hydroxymethylation levels from positive clones were assayed by 5hmC dot blot. A
63 significant reduction of 5hmC signals was shown in TKO, TET1KO, TET1/2DKO, and TET1/3DKO
64 cells, whereas TET2KO, TET3KO, and TET2/3DKO cells showed minimal alterations of 5hmC
65 levels (Supplementary Fig. 1b). To avoid functional redundancy, we focused our analysis on TKO
66 cells devoid of any TET-mediated active demethylation. Consistent with other *TET* knock-out mESC
67 and hESC lines [18,22], TKO H1-hESCs exhibited no apparent defects in stem cell self-renewal capacity
68 or expression of pluripotent factors (Supplementary Fig. 1e).

69 To determine whether TET proteins affect hESC differentiation toward pancreatic endocrine fate,
70 we used an established stepwise differentiation platform [21] to induce efficient differentiation of
71 hESCs to definitive endoderm (DE), primitive gut tube (GT), pancreatic progenitor (PP), and

72 pancreatic endocrine (PE) (Fig. 1a). Both TET triple-deficient lines (clones 2 and 6) displayed similar
73 differentiation efficiency toward endoderm germ layer as the wild-type (WT) hESC line, in which
74 over 90% of cells were $SOX17^{+}$ by day 3 of differentiation (Supplementary Fig. 1c). Moreover,
75 expression levels of other endoderm markers, such as *FOXA2*, *FOXA1*, and *CXCR4*, were unchanged
76 in TET-depleted cells compared with control cells (Supplementary Fig. 1d, e). This analysis suggests
77 that TET dioxygenases are dispensable for endoderm specification in the context of *in vitro* hESC
78 differentiation. To examine the effects of TET ablation on pancreatic commitment, we subsequently
79 examined the expression of critical pancreatic markers at the PP and PE stages. Using flow cytometry
80 to quantitate the expression of *PDX1* at the PP stage and co-expression of *PDX1* and *NKX6.1* at the
81 PE stage, we observed a substantial decrease in TET knock-out cells (Fig. 1b). These data were
82 confirmed by immunofluorescence staining and RT-qPCR analysis (Fig. 1c, Supplementary Fig. 1e).
83 Consistent with these findings, expression of the pancreatic progenitor markers *SOX9* and *PTF1A*
84 and endocrine hormones insulin, and glucagon were significantly downregulated in TKO lines (Fig.
85 1c, Supplementary Fig. 1e). Interestingly, *PAX4*, a key determinant for β-cell specification, failed to
86 induce in TET-inactivated cells, whereas expression of the α-cell determinant, *ARX*, was not affected
87 (Supplementary Fig. 1e). These results demonstrate that TETs are required for pancreatic β-cell
88 lineage specification.

89 To investigate TET-dependent global transcriptional changes during pancreatic endocrine cell
90 fate commitment, we performed transcriptome analysis of WT and TKO cells at the ES, DE, and PP
91 stages. Hierarchical clustering of genes specifically expressed at each stage revealed a remarkable
92 downregulation of PP-specific genes in TKO_PP cells, whereas ES-specific and DE-specific genes

93 showed no obvious changes in TET-deficient cells compared with WT cells (Supplementary Fig. 1f).
94 In particular, 1,173 differentially expressed genes (DEGs) were identified in TKO_PP cells (Fig. 1d,
95 Supplementary Table 1). Among them, there were 921 downregulated DEGs in TET-deficient cells,
96 including many important developmental determinants for pancreatic endocrine specification, such
97 as *PDX1*, *NKX2.2*, *NKX6.1*, *NKX6.2*, *NEUROG3*, and *PAX4*. We also observed 252 genes,
98 particularly HOX family members, which were significantly upregulated upon TET deletion,
99 suggesting that failure to differentiate into pancreatic β-cells is tightly linked to an aberrant TF
100 network. In addition, KEGG pathway analysis of the DEGs showed enrichment for terms associated
101 with maturity onset diabetes of the young (MODY) and insulin secretion (Supplementary Fig. 1g),
102 suggesting that loss of TETs impairs pancreatic endocrine formation at later stages of endoderm
103 specification.

104 **FOXA motifs are enriched at distal regulatory elements displaying decreased accessibility upon**
105 **TET deletion**. Given that our previous study demonstrated that TET-mediated cytosine oxidation is
106 strongly associated with open chromatin regions during pancreatic differentiation [21], we performed
107 ATAC-seq to evaluate chromatin accessibility landscapes in WT and TET-deficient cells. We
108 assessed differential accessible regions (DARs) between WT_PP and TKO_PP cells from a total of
109 124,322 identified ATAC peaks and found that 4.3% of ATAC peaks significantly changed upon
110 TET deletion (Supplementary Table 2). We found that loss of TET led to an overall reduction in
111 chromatin accessibility, with 5,060 DARs showing reduced accessibility and only 290 DARs showing
112 increased accessibility in TKO_PP cells (Supplementary Fig. 1h). Moreover, DARs with decreased
113 accessibility were located primarily at distal regions (> 1 kb transcription start site (TSS)) (Fig. 1e).

114 Decomposition of chromatin accessibility and DEGs in TKO_PP cells revealed that downregulated
115 genes became less accessible (Fig. 1f). To enhance the biological insights of TET depletion-mediated
116 changes in chromatin accessibility, we determined DNA binding motifs within DARs and found that
117 regions with reduced accessibility were mostly enriched for motifs of pioneer TFs essential for
118 pancreas organogenesis, such as FOXAs and GATAs [23,24] (Fig. 1g).

119 **TET deficiency induces a differentiation-associated loss of 5hmC at pioneer TF binding sites**.
120 To gain insight into the TET-mediated DNA methylation network governing pancreatic
121 differentiation, we used cytosine-5-methylenesulfonate immunoprecipitation (CMS-IP) coupled with
122 high-throughput sequencing to profile DNA hydroxymethylation landscapes in WT_PP and TKO_PP
123 cells. As a consequence of TET deletion, we found genome-wide loss of DNA hydroxymethylation
124 in TET-deficient cells (Supplementary Fig. 2a, b). 94% of CMS-positive regions showed a significant
125 reduction in TKO_PP cells relative to WT_PP cells (Supplementary Fig. 2c). These differentially
126 hydroxymethylated regions showing reduced 5hmC (hypo-DHMRs) were primarily located at non-
127 promoter regions (> 1 kb from TSS) (Supplementary Fig. 2d).

128 Reduced DNA hydroxymethylation in TET-deficient cells could be a result of initial loss of
129 5hmC at the ES stage or unsuccessful oxidation of 5mC during lineage progression. To provide
130 biological insight into development-specific changes of hydroxymethylation upon TET inactivation,
131 we systematically compared hypo-DHMRs found in TKO_PP cells to previously identified regions
132 showing increased 5hmC during differentiation of hESCs toward pancreatic endoderm [21].
133 Specifically, 27,113 hypo-DHMRs with higher 5hmC levels in WT_PP cells than in WT_ES cells
134 (named 'differentiation-specific hypo-DHMRs') were first isolated from a total of 70,857 TKO hypo-

135 DHMRs (Fig. 2a). We subsequently clustered them into four categories based on the dynamic changes
136 of 5hmC across stages (Fig. 2b). In particular, one group gained 5hmC specifically at the PP stage
137 (PP-specific), whereas others gained 5hmC at the earlier DE (DE-to-PP) or GT (GT-to-PP) stages
138 and sustained hydroxymethylation until the PP stage. We found that GATA motifs were mostly
139 associated with the DE-to-PP cluster, in which gain of 5hmC began at the DE stage (Fig. 2c, purple).
140 By contrast, the PP-specific cluster displayed a prominent presence of binding sites for HNF6,
141 which is critical for pancreatic endocrine differentiation [25] (Fig. 2c, red). Most notably, FOXA motifs
142 were predominantly associated with the GT-to-PP(h) cluster in which 5hmC levels increased at the
143 GT stage and continued to be elevated until the PP stage (Fig. 2c, blue), whereas both FOXA and
144 GATA motifs were highly associated with the GT(h)-to-PP cluster in which 5hmC peaked at the GT
145 stage and subsequently decreased at the PP stage (Fig. 2c, brown). These results suggest a unique
146 temporal binding pattern of GATAs, FOXAs, and HNF6s associated with the dynamic distribution
147 of 5hmC during pancreatic differentiation, which is supported by a recent study demonstrating
148 sequential requirements for these TFs during transitions in pancreas development [4].
149 It was previously demonstrated that the pioneer TF FOXA2 is essential for enhancer priming and
150 chromatin remodeling during pancreatic differentiation [3,4]. By analyzing FOXA2-binding datasets
151 previously generated [4] from a similar stepwise pancreatic differentiation system, we found that
152 binding of FOXA2 corresponded well with the dynamic changes of 5hmC across differentiation
153 stages in the four 'differentiation-specific hypo-DHMRs' clusters (Fig. 2d). These results suggest that
154 TET-mediated hydroxymethylation strongly correlates with FOXA2 deposition during development.
155 Given our previous finding that 5hmC is positively associated with chromatin accessibility and

156 enhancer activity [21], we hypothesized that loss of TET inhibits chromatin opening and enhancer
157 activation at FOXA2 targets during pancreatic differentiation. Thus, we conducted ChIP-seq for
158 enhancer signatures H3K4me1 and H3K27ac in WT_PP and TKO_PP cells and performed integrated
159 analysis. We found remarkable decreases in ATAC and H3K27ac signals on FOXA2 targets
160 overlapping with 'differentiation-specific hypo-DHMRs' upon TET deletion (Fig. 2e), particularly at
161 distal regions (Supplementary Fig. 2e). Moreover, ATAC, H3K4me1, and H3K27ac signals were
162 substantially higher at FOXA2/hypo-DHMR-coexisting sites in pancreatic progenitors (Fig. 2e),
163 suggesting that 5hmC-associated FOXA2 targets are predominantly enriched for active chromatin.
164 Nevertheless, FOXA and GATA family members were expressed at similar levels in TKO and WT
165 cells (Supplementary Fig. 2f), suggesting that inhibition of TET did not alter the expression levels of
166 pioneer TFs. Collectively, these data reveal that TET deficiency results in a progressive failure of
167 5mC oxidation at a subset of FOXA2 targets essential for the establishment of active chromatin
168 during differentiation.

169 **Pancreas-specific DMRs feature reduced chromatin activity during differentiation**. To
170 investigate TET deficiency-mediated alterations in global DNA methylation, we performed whole-
171 genome bisulfite sequencing (WGBS) in WT_PP and TKO_PP cells. Over 86% of sequencing reads
172 were uniquely aligned to hg38 with a high sequencing depth of 24 × on CpG dinucleotides and typical
173 bimodal distribution of methylation ratio in each sample (Supplementary Fig. 3a, b). The methylation
174 ratio (5mC/C) was depleted at TSS but enriched across gene coding regions, especially within
175 TKO_PP cells (Supplementary Fig. 3c). Among 26.6 million CpG sites detected in both WT_PP and
176 TKO_PP cells (depth ≥ 5), a total of 251,658 differentially methylated cytosines (DMCs; credible

177 difference of methylation ratio > 20%) were identified (Fig. 3a). Strikingly, 97.5% of DMCs were
178 hypermethylated (hyper-DMCs), suggesting that TET inhibition results in a pronounced gain of
179 methylation during pancreas differentiation. We observed enrichment of DMCs primarily at
180 intergenic regions and introns (Supplementary Fig. 3d), whereas substantial enrichment of hypo-
181 DMCs was also found in repeat elements, such as long interspersed elements, consistent with a
182 suggested connection between hypomethylation and activation of transposable elements [26,27]. Based
183 on an established link between DNA methylation and transcription regulation, we further calculated
184 changes in methylation levels on cis-regulatory elements previously identified in pancreatic
185 progenitors [3,28]. We found increased methylation at bivalent promoters, active enhancers, and, to a
186 lesser extent, poised enhancers (Fig. 3b). Notably, hypermethylation was preferentially enriched at
187 open chromatin (ATAC) as well as FOXA2, GATA4, GATA6, and PDX1 binding regions located
188 distally (Fig. 3b, Supplementary Fig. 3e). This analysis demonstrates that active regulatory elements
189 are hypermethylated upon TET depletion during pancreatic differentiation.

190 Our previous studies reveal that DNA demethylation is correlated with pancreatic endocrine
191 patterning [21]. To gain better insight into the role of TET-mediated methylation changes in pancreatic
192 differentiation, we analyzed differentially methylated regions (DMRs) by connecting at least three
193 consecutive DMCs [29] between TKO_PP and WT_PP cells. We found a total of 16,490 hyper-DMRs
194 and classified them into two categories based on their 5mC levels in pancreatic progenitors versus
195 hESCs [30] (Fig. 3c). Notably, more than half (n = 10,254) of hyper-DMRs exhibited less 5mC in
196 WT_PP cells than in hESCs (named pancreas-specific hyper-DMRs), whereas the others (n = 6,236)
197 showed similar methylation levels (non-pancreas hyper-DMRs) (Fig. 3c, Supplementary Fig. 3f).

198 Interestingly, we found that FOXA2, GATA4, and GATA6 were predominantly enriched at pancreas-
199 specific hyper-DMRs in pancreatic progenitors (Fig. 3d), suggesting that TET-dependent
200 demethylation is primarily associated with pioneer TF binding. We further compared ATAC,
201 H3K4me1, and H3K27ac signals at pancreas-specific hyper-DMRs with those at non-pancreatic
202 hyper-DMRs. We found that chromatin activity was markedly reduced in TET-deficient cells at
203 distally located hyper-DMRs in the pancreatic-specific group (Fig. 3e, Supplementary Fig. 3g).
204 Consistently, genomic loci displaying decreased accessibility showed a substantial increase in DNA
205 methylation upon depletion of TET (Fig. 3f). For example, we detected significant hypermethylation
206 at the distal regulatory elements of *PTF1A* and *NKX2.2* loci (Supplementary Fig. 3h). Altogether,
207 these analyses demonstrate that TET-dependent demethylation at enhancers and other distal
208 regulatory elements is essential for chromatin remodeling during pancreas development.

209 Additionally, we found that 774 type 2 diabetes (T2D)-associated islet hyper-DMRs, which were
210 recently identified [31], overlapped with hyper-DMRs found in TET-deficient cells (Supplementary
211 Table 3). Remarkably, four of the most significant T2D-associated islet hyper-DMRs annotated to
212 the *PDX1* and lncRNA *PDX1-AS1* loci were hypermethylated upon TET deletion during pancreatic
213 differentiation (Fig. 3g, green areas). We also uncovered an adjacent hyper-DMR (Fig. 3g, pink area)
214 that overlapped with the pioneer TF binding sites and showed decreased ATAC, H3K4me1, and
215 H3K27ac signals in a TET-dependent manner. Given that both *PDX1* and *PDX1-AS1* are
216 downregulated in islets from donors with T2D [32], these data suggest that TET inactivation leads to
217 remarkable DNA hypermethylation featuring loss of chromatin activity at regulatory elements, which
218 might be crucial for the development of diabetes.

219 **TET1 is required in pancreatic β-cell specification**. Our findings suggest that TET inactivation-
220 induced aberrant methylation/hydroxymethylation at least in part contributes to defective β-cell
221 specification. To determine the essential role of each TET family member in pancreatic differentiation,
222 we further analyzed mutants with single (*TET1*, *TET2*, or *TET3*) or double (*TET1/2*, *TET2/3*, or
223 *TET1/3*) *TET* knock-out. All mutant lines were able to induce the expression of *PDX1* and *NKX6.1*
224 to levels comparable to WT (Supplementary Fig. 4a). However, only those retaining intact *TET1*
225 expression (TET2KO, TET3KO, and TET2/3DKO) displayed proper induction of *PAX4* (Fig. 4a). In
226 comparison with *TET2*/*TET3* double-deletion, inhibition of TET1 alone had significant effects on the
227 formation of INS- and C-peptide (CPEP)-expressing β-cells but not GCG-expressing α-cells (Fig. 4b,
228 Supplementary Fig. 4b). To further determine whether TET1 is responsible for β-cell induction, we
229 restored *TET1* expression using lentivirus-mediated gene transduction to TET-depleted hESCs.
230 *TET1*-repaired TKO cells showed a global increase in 5hmC levels, confirming the replenishment of
231 hydroxymethylation (Supplementary Fig. 4c). Differentiation of the TKO-TET1 line toward
232 pancreatic endocrine fate led to robust restoration of β-cell genes, including *NKX6.1*, *PAX4*, *INS*, and
233 *CPEP* (Fig. 4c, d, Supplementary Fig. 4d), suggesting that TET1 is critical for β-cell specification.
234 To evaluate global transcriptome changes in response to *TET1* deletion, we performed RNA-seq
235 of TET1KO cells at the PP stage. Integrated analysis of WT_PP, TKO_PP, and TET1KO_PP data
236 revealed a total of 1,590 DEGs among the three lines (Supplementary Table 4). Specifically, 555
237 genes, including most pancreas developmental regulators such as *PDX1*, *SOX9*, *NKX2.2*, *NKX6.1*,
238 *NEUROD1*, and *PAX6*, were downregulated in TKO_PP cells but not in TET1KO_PP cells (Fig. 4e),
239 consistent with effective differentiation of TET1KO-hESCs into $PDX1^{+}/NKX6.1^{+}$ cells

240 (Supplementary Fig. 4a). However, 536 genes, including the β-cell fate determinants *PAX4*, *NKX6.2*,
241 and *FEV* [33-35], were significantly inhibited in TET1-deficient cells, implicating TET1 as responsible
242 for the activation of a subset of genes essential for β-cell identity. To further analyze the functional
243 consequences of TET1 inhibition, WT-, TET1KO-, and TKO-hESCs were differentiated to the PE
244 stage and subsequently engrafted into SCID-beige mice under the kidney capsules (Fig. 4f). Glucose-
245 stimulated human C-peptide secretion was determined 18 weeks post-transplantation. Notably, mice
246 engrafted with WT_PE cells produced substantial fasting C-peptide in serum (1605 ± 527 pg/ml) and
247 showed statistically significant glucose-stimulated C-peptide secretion (2,358 ± 839 pg/ml). By
248 contrast, mice transplanted with TET1KO_PE cells secreted extremely low amounts of basal C-
249 peptide (163 ± 122 pg/ml) and showed no response to glucose stimulation (149 ± 161 pg/ml). In
250 agreement with these functional results, excised WT_PE cell grafts were highly composed of insulin^{+}
251 β-cells (Supplementary Fig. 4e). The TET1KO_PE cell grafts displayed much less insulin content,
252 and only the δ-cell hormone somatostatin was detected in TKO_PE cell grafts. Together, these data
253 demonstrate that loss of TET1 impairs β-cell specification and maturation.

254 **TET1 binding sites are distinct in pancreatic progenitors**. To identify the direct targets of TET1,
255 we performed ChIP-seq for TET1 in pancreatic progenitors and identified a total of 8,476 peaks with
256 higher signals around TSSs (Supplementary Fig. 5a). Consistent with previous reports [18,36], TET1
257 was enriched at CpG islands (Supplementary Fig. 5b) and was primarily associated with
258 unmethylated genomic loci (Fig. 5a). To further examine the epigenetic features of TET1 target sites
259 in pancreatic progenitors, we centered all TET1 peaks and analyzed their accessibility, 5hmC, and
260 deposition of H3K4me1, H3K27ac, H3K4me3 [28], and H3K27me3 [28]. We found that TET1 binding

261 sites predominantly overlapped with active chromatin modifications at proximal (Fig. 5b, left panel)
262 and distal (Fig. 5b, right panel) regions, suggesting that TET1 is primarily present at active regulatory
263 elements in pancreatic progenitors.

264 Recent studies show that TET1 safeguards bivalent promoters in ESCs to ensure proper neuronal
265 differentiation [18]. Therefore, it is interesting to examine whether TET1 occupies similar or different
266 loci upon hESC differentiation toward pancreatic endoderm. We compared TET1 binding sites
267 identified in pancreatic progenitors and pluripotent stem cells using TET1 ChIP-seq data previously
268 generated from hESCs [18]. 4,463 TET1 peaks specific to pancreatic progenitors were referred to 'PP-
269 specific', 22,177 binding sites specific to hESCs were called 'ES-specific', and 4,013 TET1 sites
270 shared between the two groups were named 'common' (Fig. 5c). We then analyzed the annotations
271 of their nearby genes with Genomic Regions Enrichment of Annotations Tool (GREAT) and found
272 that only PP-specific peaks were enriched for terms of endocrine pancreas development
273 (Supplementary Fig. 5c). In agreement with these findings, PP-specific sites prominently featured
274 FOXA2 and CTCF motifs, whereas insulator CTCF and its paralogue BORIS motifs were mostly
275 enriched at ES-specific sites (Fig. 5d). This analysis suggests that TET1 is involved in different
276 biological functions in ESCs and lineage-committed cells. Interestingly, in contrast to the PP-specific
277 sites, most of which were distally located (Fig. 5e), the 'common' TET1 binding sites were mainly
278 located at proximal promoters and enriched for gene ontology annotations connected to essential
279 biological processes, such as mRNA processing, biosynthesis, and translation (Supplementary Fig.
280 5c). We further examined chromatin accessibility and histone modifications of promoter and
281 enhancer regions at proximal and distal TET1 binding sites. We found that TET1 bound more strongly

282 at both proximal and distal 'common' sites than at 'PP-specific' sites (Fig. 5f, TET1). Higher active
283 chromatin signals were also observed at the proximal (Fig. 5f, ATAC and H3K4me3) and distal (Fig.
284 5f, ATAC and H3K27ac) 'common' sites. The more active chromatin modifications at 'common'
285 TET1 targets may contribute to maintaining continually active transcripts essential for basic
286 biological functions in different types of cells. By contrast, cell-type-specific TET1 binding may
287 participate in chromatin remodeling during lineage specification.

288 Recent studies demonstrate that FOXA2 triggers chromatin opening on a subset of its potential
289 binding sites during endoderm differentiation [37]. In the present study, we found that FOXA2 target
290 sites acquiring 5hmC during pancreatic differentiation correlate with high levels of active chromatin
291 modifications (Fig. 2). We thus hypothesized that TET1 binds to a specific set of FOXA2 targets
292 associated with unique chromatin features. We isolated FOXA2 binding sites in pancreatic
293 progenitors [4] and analyzed DNA methylation, chromatin accessibility, and enhancer activity with or
294 without TET1 binding. The functional relevance of TET1 and FOXA2 co-binding is supported by
295 exceptionally low levels of methylation as well as more active chromatin modifications (ATAC,
296 H3K4me1, and H3K27ac), particularly at distal regions (Fig. 5g, Supplementary Fig. 5d). Moreover,
297 only the loci bound by both FOXA2 and TET1 were significantly enriched for terms associated with
298 pancreas development (Supplementary Fig. 5e), implicating a unique feature of TET1/FOXA2 co-
299 binding elements. Taken together, our data suggest that TET1 binds to a specific subset of FOXA2
300 targets that are confined mainly to active regulatory compartments during pancreatic differentiation.

301 **TET1 is required for the *PAX4* enhancer to achieve a hypomethylated state**. As TET1 depletion
302 inhibited the induction of genes essential for β-cell specification (Fig. 4), we reasoned that co-binding

303 of TET1 and FOXA2 at distal regulatory elements modulates focal DNA
304 methylation/hydroxymethylation and subsequent gene activation. To identify potential TET1
305 regulatory elements, we integrated gene expression, chromatin accessibility, and TET1/FOXA2
306 binding profiles into a comprehensive analysis. We found that a putative *PAX4* enhancer (~4.0 kb
307 upstream of the TSS), where TET1/FOXA2 co-bound, displayed hypermethylation and decreased
308 accessibility in TET-deficient cells (Fig. 6a, pink area). We next examined whether the deletion of
309 TET1 alone results in hypermethylation at this site. Locus-specific methylation was determined in
310 TET1KO_PP, TET2/3DKO_PP, TKO_PP, and WT_PP cells using a glucosylation and digestion-
311 based method followed by qPCR analysis with two independent pairs of primers (PAX4-P1 and
312 PAX4-P2) located within the TET1/FOXA2 co-binding site (Fig. 6a). Notably, the percentage of
313 5mC was increased to 35–50% for TET1KO and 60–65% for TKO compared with WT but remained
314 unchanged for TET2/3DKO (Fig. 6b, left panel). A corresponding decrease in unmethylated cytosine
315 content was observed, with values of 45–65% and ~35% of C in TET1KO and TKO samples,
316 respectively (Fig. 6b, right panel). As a housekeeping control, we examined methylation content at a
317 nearby region using the PAX4-P3 primer, and, as expected, no significant differences in 5mC and C
318 were observed in any samples.

319 Furthermore, we determined methylation contents at the same *PAX4* locus in TET1-repaired
320 TKO cells. Consistent with the results found in TET2/3DKO cells, no detectable differences in 5mC
321 and C were found among TKO-TET1 samples (Supplementary Fig. 6). Together with the increased
322 expression of *PAX4* in TKO-TET1 cells (Fig. 4d), we conclude that TET1 is responsible for the
323 establishment or maintenance of a hypomethylated state at the *PAX4* enhancer, which is essential for

324 transcription activation of *PAX4*.

325 **Discussion**

326 In the present work, we dissected the roles of TET proteins in pancreatic endocrine commitment
327 based on a stepwise hESC differentiation system. We found that the loss of all three TET family
328 members significantly impaired the differentiation of pancreatic β-cells. Furthermore, we discovered
329 that locus-specific hypermethylation was associated with genes essential for β-cell specification and
330 maturation, such as *PAX4* [33], *PDX1* [38], and *NKX2.2* [39]. The reintroduction of *TET1* in TET-deficient
331 cells effectively reversed hypermethylation and restored the expression of *PAX4*. We further
332 demonstrated that TET1 functions as an upstream epigenetic regulator of *PAX4* through direct
333 binding at a putative *PAX4* enhancer to preserve its unmethylated status, thereby potentiating *PAX4*
334 expression to adopt β-cell fate during endocrine lineage commitment. Consistently, we observed
335 striking increases in methylation at the *PAX4* enhancer in TET1 knock-out cells but not in
336 TET2/TET3 DKO cells, suggesting that TET1 epigenetically regulates induction of the β-cell
337 program in a locus-specific manner. Moreover, despite the successful induction of *PDX1* and *INS*
338 upon deletion of TET1 alone, mice receiving TET1KO cell grafts showed a persistent defective
339 insulin response to glucose, implying that TET1 is also essential for β-cell maturation.

340 Whereas the specification of β-cells was strongly influenced by depletion of *TET1*, we did not
341 observe a significant impact on the expression of *ARX*, a critical α-cell fate determinant [40]. In contrast
342 to *PAX4*, no hyper-DMRs were identified within the *ARX* locus, where methylation levels were nearly
343 undetectable in pancreatic progenitors. Previous studies demonstrate that several CpG-rich sites of
344 *Arx*, including one site close to TSS and another site 2 kb upstream of TSS, are heavily methylated

345 in adult β-cells but not α-cells [41]. Moreover, pharmacological inhibition of DNA methyltransferases,
346 *Dnmts*, in pancreatic progenitors promotes α-cell specification [42], whereas deletion of *Dnmt1* in β-
347 cells results in demethylation and depression of *Arx* [41]. We thus speculate that *ARX* is hypomethylated
348 in pancreatic progenitors in a TET-independent manner. The *ARX* locus maintains an unmethylated
349 state when progenitors differentiate into α-cells, whereas it becomes hypermethylated once cells
350 commit to β-cell fate in the presence of DNMTs and other β-cell-specific factors. In line with this
351 hypothesis are findings that Nkx2.2 recruits Dnmt3a to the *Arx* promoter to repress its expression in
352 β-cells [43]. In the future, it will be interesting to explore whether there are differences in the complete
353 epigenetic landscapes of endocrine progenitors, which subsequently differentiate into α- or β-cells.
354 TET dioxygenases are critical for lineage induction in a cell-type-specific manner [44]. How TETs
355 recognize lineage-specific regulatory elements and modulate chromatin remodeling during pancreas
356 development remains unknown. Here, we addressed these questions by performing analyses
357 integrating gene expression with multiple chromatin features, including DNA methylation,
358 hydroxymethylation, chromatin accessibility, and histone modifications of promoters and enhancers.
359 We found extensive hypermethylation in TET-deficient cells that differentiated to the pancreatic
360 progenitor stage. A significant portion of hyper-DMRs were distributed in a cell-type-specific manner,
361 in which they were enriched for the binding of FOXA2, a pioneer TF essential for pancreatic
362 endoderm differentiation, and showed remarkable decreases in chromatin activity upon TET
363 inactivation. It is noteworthy that we unveiled a unique TF binding pattern associated with a stepwise
364 increase of 5hmC during pancreatic differentiation. The presence of GATA, FOXA, and HNF6
365 binding motifs in a temporal manner suggests that TET proteins are recruited to chromatin by a set

366 of lineage-specific TFs sequentially expressed during pancreatic differentiation. More intriguingly,
367 nearly 800 hyper-DMRs recently identified in T2D pathogenesis [31] overlapped with hyper-DMRs
368 found in TET-deficient cells in the present study, implying that TET dioxygenases are crucial for β-
369 cell function.

370 During lineage specification, chromatin structure is dynamically changed between 'closed' and
371 'open' states. Open chromatin regions such as primed and active enhancers are accessible for TF and
372 epigenetic modulator binding to initiate gene transcription. Proper chromatin remodeling is believed
373 to be at least partly triggered by pioneer TFs, which can directly bind to nucleosomal DNA [6]. It was
374 previously suggested that pioneer TF FOXA2 initiates chromatin remodeling and enhancer priming
375 during pancreatic differentiation [3,4]. Interestingly, our analyses revealed that changes in 5hmC mirror
376 the dynamic binding of FOXA2 in cells differentiated from hESCs through defined lineage
377 intermediates toward pancreatic endocrine fate. We showed that chromatin activity was markedly
378 decreased at the FOXA2 binding sites associated with DHMRs in TET-deficient cells, suggesting
379 that lineage-specific hydroxymethylation is processed at a subset of FOXA2 target sites to influence
380 chromatin opening.

381 How pioneer TFs initiate chromatin opening is still mostly unknown. One suggestion is that
382 FOXA2 can recruit nucleosome remodeling complexes SWI/SNF to alter the surrounding chromatin
383 structure [45]. Our present study demonstrates that TET1 binds to two distinct groups of regulatory
384 elements: universal and lineage-specific TET1 sites. The fact that 1) pancreatic progenitor-specific
385 TET1 targets are enriched for the FOXA2 binding motif and 2) co-occupancy of TET1 and FOXA2
386 at distal regulatory elements is associated with more active chromatin suggests that TET1 residing in

387 specific genomic loci modulates FOXA2-mediated chromatin opening. Several studies suggest that
388 TET can be directly recruited by pioneer TFs, such as FOXA1 and PU.1, to lineage-specific enhancers
389 to facilitate local demethylation and gene induction [46,47]. However, a recent study found that
390 chromatin opening requires cooperative binding of FOXA2 and additional TFs, such as GATA4,
391 during endoderm differentiation [37]. This suggests complex cross-talk between pioneer TFs and
392 chromatin remodelers in endodermal lineage specification. Further investigation is warranted to
393 determine whether TET1 is recruited to distinct FOXA2-binding sites by lineage-specific TFs to
394 synergistically regulate chromatin remodeling.

395 **Methods**

396 **Cell lines.** The human embryonic stem cell line H1 was obtained from WiCell Research Institute. H1
397 cells were maintained on Matrigel (Corning) in mTeSR1 (STEMCELL Technologies) and passaged
398 every for 4-5 days using 0.5 mM EDTA and 3 mM NaCl. Mycoplasma detection was regularly
399 performed by the Stem Cell Core Facility at the University of Macau.

400 **Pancreatic differentiation.** All differentiation experiments were repeated at least three times with
401 three individual clones of the same phenotype. Pancreatic differentiation was performed as previously
402 described with slight modifications [48]. In brief, hESCs were dissociated with Accutase (eBioscience)
403 and seeded at a density of 19,000 cells/cm^2 on Matrigel in mTeSR1 supplemented with 10 μM Rho-
404 associated protein kinase inhibitor Y-27632 (Miltenyi Biotec). Upon reaching 95% confluence, cells
405 were exposed to differentiation medium with daily media feeding.

406 ES-to-DE (3 d): hESCs were exposed to 100 ng/ml Activin A (PeproTech) and 25 ng/ml Wnt-3a
407 (PeproTech) in basal medium-I containing MCDB 131 medium (Gibco), 1.5 g/l $NaHCO_3$, 1×

408 GlutaMAX (Gibco), 10 mM glucose, and 0.5% BSA for 1 day. For 2 additional days, cells were
409 cultured in basal medium-I further supplemented with 100 ng/ml Activin A.

410 DE-to-GT (3 d): DE intermediates were incubated in basal medium-I supplemented with 50
411 ng/ml FGF7 (PeproTech) for 3 days.

412 GT-to-PP (5 d): GT intermediates were cultured for 3 days in basal medium-II containing MCDB
413 131 medium, 2.5 g/l $NaHCO_3$, 1× GlutaMAX, 10 mM glucose, 2% BSA, and 1:200 ITS-X (Gibco),
414 which was further supplemented with 50 ng/ml FGF7, 0.25 μM hedgehog inhibitor SANT-1 (Sigma),
415 1 μM retinoic acid (Sigma), 100 nM BMP inhibitor LDN193189 (Stemgent), and 200 nM PKC
416 activator TPB (Millipore). After 3 days of culture, cells were treated for 2 days with 2 ng/ml FGF7,
417 0.25 μM SANT-1, 0.1 μM retinoic acid, 200 nM LDN193189, and 100 nM TPB in basal medium-II.

418 PP-to-PE (3 d): PP intermediates were differentiated in basal medium-III containing MCDB 131
419 medium, 1.5 g/l $NaHCO_3$, 1× GlutaMAX, 20 mM glucose, 2% BSA, and 1:200 ITS-X, which was
420 further supplemented with 0.25 μM SANT-1, 0.05 μM retinoic acid, 100 nM LDN193189, 1 μM T3
421 (3,3',5-Triiodo-L-thyronine sodium salt, Sigma), 10 μM ALK5 inhibitor II (Enzo Life Sciences), 10
422 μM $ZnSO_4$, and 10 μg/ml heparin (Sigma).

423 **Animal experiments.** All animal experiments were approved by the University of Macau Animal
424 Ethics Committee. Immunocompromised SCID-beige mice were obtained from Charles River and
425 maintained under a 12-h light/dark cycle with free access to standard mouse diet. For transplantation,
426 ~5 million hESC-derived d14 cells were enzymatically dissociated and aggregated using ultra-low
427 adherent plates (Corning) in basal medium-III further supplemented with 100 nM LDN193189, 1 μM
428 T3, 10 μM ALK5 inhibitor II, 10 μM $ZnSO_4$, 100 nM γ-secretase inhibitor XX (Millipore), and 10
429 μM Y-27632 for 1 day. Cell aggregates were then transplanted into 6-week-old SCID-beige mice

430 under the kidney capsule as previously described [49].

431 Glucose-stimulated human C-peptide secretion was assessed with mice 18 weeks post-
432 transplantation. Blood samples were collected after overnight fasting and 30 min following an
433 intraperitoneal injection of glucose (2 g/kg body weight). Human C-peptide levels in isolated plasma
434 were quantified using the STELLUX Chemi Human C-peptide ELISA kit (ALPCO Diagnostics)
435 according to the manufacturer's instructions.

436 **Generation of *TET* knock-out lines**. *TET* knock-out hESCs were generated using CRISPR/Cas9
437 technology. gRNAs (Supplementary Table 5) were designed to target the sequences encoding exon 7
438 of *TET1*, exon 3 of *TET2*, or exon 3 of *TET3* and cloned into pX330 vector (Addgene #42230) as
439 previously described [50]. Constructs containing validated gRNAs were electroporated together with a
440 vector expressing puromycin into hESCs using the P3 Primary Cell 4D-Nucleofector X kit (Lonza)
441 following the manufacturer's instructions. The electroporated cells were plated at ~2,000 cells/cm^2
442 and cultured on Matrigel in mTeSR1 supplemented with 10 μM Y-27632 for 2 days. Successfully
443 transfected cells were selected with 1 μg/ml puromycin in mTeSR™1 and allowed to expand to form
444 visible colonies from a single cell. Subsequently, clonal colonies were manually picked and reseeded
445 individually into 24-well plates. The amplified colonies were analyzed by Sanger sequencing at
446 targeted loci for the presence of Indel mutations.

447 **TET1 expression cell lines**. TET1 lentivirus expression plasmid was constructed by amplifying the
448 human *TET1* ORF from FH-TET1-pEF (Addgene #49792) and inserting it into *KpnI* and *BamHI* sites
449 of the lentiCRISPR v2 vector (Addgene #52961). Lentivirus particles were prepared as previously
450 described [51]. For viral transduction, TKO-hESCs were grown on Matrigel in mTeSR1 using 24-well

451 plates and treated with 6 μg/ml polybrene for 15 min at 37°C. Concentrated lentivirus particles (10
452 μl, 1×10^6 TU/ml) were added to cell culture and incubated overnight at 37°C. On the next day, viral
453 infection was repeated (30 μl, 1×10^6 TU/ml) to increase transduction efficiency. Infected cells were
454 cultured in mTeSR1 for 2 days and then exposed to 1 μg/ml puromycin for 10 days. The TKO line
455 TKO-TET1, in which an intact *TET1* cDNA was expressed, was amplified and frozen down. Control
456 cells (TKO-CRTL) carrying the lentiCRISPR v2 plasmid were established with the same
457 experimental procedure.

458 **Locus-specific detection of 5mC**. Detection of 5mC content at particular CCGG sites was performed
459 using the Epimark 5hmC and 5mC analysis kit (New England Biolabs) following the manufacturer's
460 instructions. Briefly, genomic DNA was extracted using the DNeasy Blood and Tissue kit (Qiagen)
461 followed by RNase treatment. RNase-treated DNA samples were incubated with T4 β-
462 glucosyltransferase at 37°C for 16 h. The glycosylated DNA was subsequently digested with *MspI* or
463 *HpaII* for 8 h at 37°C. Samples were treated with Proteinase K at 40°C for 30 min and then at 95°C
464 for 10 min to inactivate the enzymes. Site-specific methylation contents were examined by RT-qPCR
465 using the primers listed in Supplementary Table 6. The percentage of 5mC and unmodified cytosine
466 were calculated using the comparative C_t method.

467 **5hmC dot blot assay**. Genomic DNA was extracted using the DNeasy Blood and Tissue kit (Qiagen)
468 according to the manufacturer's instructions. DNA was denatured in 1 M NaOH supplemented with
469 25 mM EDTA at 95°C for 10 min and then neutralized with 2 M ice-cold ammonium acetate for 10
470 min. Two-fold serial dilutions of the DNA samples were spotted onto nitrocellulose membrane. The
471 air-dried membrane was fixed with UV irradiation (CL-1000 UV crosslinker, Ultra-Violet Products),

472 blocked with 5% non-fat milk, and incubated with a rabbit anti-5hmC antibody (1:10,000, Active
473 Motif) followed by an HRP-conjugated anti-rabbit antibody (1:5,000, Jackson ImmunoResearch).
474 Signal was visualized with SuperSignal West Pico PLUS chemiluminescent substrate (Thermo
475 Fisher Scientific). The same membrane was subsequently stained with 0.02% methylene blue in 0.3
476 M sodium acetate to ensure equal loading of input DNA.

477 **RNA isolation for real-time quantitative PCR**. Total RNA was extracted using the RNeasy Plus
478 Mini kit (Qiagen) according to the manufacturer's instructions. cDNA was synthesized using the
479 PrimeScript RT reagent kit (Takara). Real-time quantitative PCR was performed in triplicate using
480 the SYBR Premix Ex Taq (Tli RNase H Plus) kit (Takara). The expression of *TBP* was used for the
481 normalization of mRNA expression. All primers used for RT-qPCR were listed in Supplementary
482 Table 6.

483 **Immunocytochemical analysis**. Differentiated cells were fixed in 4% paraformaldehyde for 30 min
484 at room temperature, washed, and then permeabilized with 0.15% Triton X-100 at room temperature
485 for 1 h. Following blocking with 5% normal donkey serum (Jackson Immuno Research Laboratories),
486 samples were incubated with primary antibodies at 4°C overnight and then appropriate secondary
487 antibodies for 1 h at room temperature. Images were acquired using the Zeiss Axio Observer
488 microscope. For transplant grafts, tissues were fixed with 4% paraformaldehyde overnight at 4°C,
489 washed with PBS, and subsequently exposed to 30% sucrose overnight at 4°C. Samples were
490 mounted with Optimal Cutting Temperature Compound (Tissue-Tek) and sectioned at 10 μm.
491 Immunofluorescent staining was performed on cryosections as described above. Antibodies used for
492 immunofluorescent staining are listed in Supplementary Table 7.

493 **Flow cytometry analysis.** Cells were enzymatically dissociated into single cells and fixed with 4%
494 paraformaldehyde for 20 min at 4°C. Fixed cells were permeabilized with Perm/Wash Buffer (BD
495 Biosciences) and stained with primary antibodies (Supplementary Table 7) diluted in Perm/Wash
496 Buffer overnight at 4°C. Cells were subsequently washed, stained with appropriate secondary
497 antibodies for 1 h at room temperature, and assessed using an Accuri C6 flow cytometer (BD
498 Biosciences). Data were analyzed using FlowJo software (TreeStar).
499 **RNA-seq library construction and data analysis.** Total RNA was isolated using Trizol reagent
500 following the manufacturer's instructions. RNA integrity was determined using an Agilent 2100
501 Bioanalyzer (Agilent Technologies). Subsequently, polyA-tailed RNA was selected using Dynabeads
502 oligo(dT) (Thermo Fisher Scientific), and libraries were prepared using the NEBNext Ultra RNA
503 Library Prep kit for Illumina (New England Biolabs). Libraries were subjected to high-throughput
504 sequencing on an Illumina HiSeq 2500 system (150 bp, paired-end) at Novogene (Tianjin, China).
505 To process the sequencing data, low-quality bases and adaptor were trimmed using TrimGalore
506 v.0.5.0 (options: --quality 20 and --length 50, https://github.com/FelixKrueger/TrimGalore). Clean
507 reads were aligned to the hg38 reference genome using STAR v.2.5.3 [52] with default parameters, and
508 only uniquely mapped reads were used for downstream analysis. A count matrix for each gene was
509 generated using htseq-count (HTSeq package [53]). DESeq2 [54] was used to identify significant DEGs
510 in knock-out samples compared with WT samples at different differentiation stages (fold change (FC)
511 ≥ 2; False Discovery Rate (FDR) < 0.05). Hierarchical cluster analysis [55] of the union DEGs was used
512 to determine stage-specific signature genes. The 'ClusterProfilter' package in R [56] was used for the
513 functional enrichment analysis of DEGs in KEGG pathways.

514 **ATAC-seq library preparation and data analysis**. ATAC-seq libraries were prepared as previously
515 described [57]. In brief, cells were enzymatically dissociated and lysed in lysis buffer (10 mM Tris-HCl,
516 pH 7.4, 10 mM NaCl, 3 mM MgCl2, 0.1% IGEPAL CA-630). Immediately after centrifugation,
517 transposition reactions were carried out by adding Tn5 transposes from the Illumina Nextera DNA
518 library preparation kit to the isolated nuclei and incubation at 37°C for 30 min. DNA fragments were
519 purified using the MinElute PCR Purification kit (Qiagen) and amplified using the KAPA real-time
520 library amplification kit (Roche). Libraries were purified using PCRClean DX beads (Aline
521 Biosciences) and subsequently subjected to high-throughput sequencing on an Illumina NextSeq 500
522 instrument (75 cycle, paired-end).

523 Adaptor trimming of raw reads was performed using TrimGalore v0.5.0 (options: --quality 20
524 and --length 20), and high-quality (Q ≥ 20) reads were uniquely aligned to the hg38 reference genome
525 using Bowtie2 with the '--very-sensitive' option. Reads mapped to mitochondrial DNA and PCR
526 duplicate reads were removed, and uniquely mapped reads were extracted for downstream analysis.
527 Genrich v.0.5 (https://github.com/jsh58/Genrich) with ATAC-seq mode (option: -j,-q 0.01) was
528 applied for each sample (with two biological replicates) to call ATAC peaks. In total, 52,817 and
529 38,697 peaks were detected in WT_PP and TKO_PP cells, respectively. Bedtools intersect was used
530 to count the reads falling into 124,322 non-overlapping peak regions, and significant DARs were
531 detected using DESeq2 by the criteria FC≥ 2 and FDR < 0.05. Volcano plots were generated using
532 the R package ggplot2. Motif annotation of DARs was performed using HOMER software [58].

533 **CMS-IP-seq library preparation and data analysis.** CMS-IP-seq libraries were performed as
534 previously described with minor modifications (Huang et al., 2012). Purified genomic DNA (with 5%

535 mouse DNA and 0.5% lambda DNA spike-in) was sheared to 200–500 bp fragments using a M220
536 Focused-ultrasonicator (Covaris). Bisulfite-converted DNA libraries with methylated adapters were
537 enriched using an in-house anti-CMS antibody bound to protein A/G Dynabeads. Amplified libraries
538 were purified by AmpuXP beads (Beckman Coulter) and then sequenced using the Illumina NextSeq
539 (75 and 40 cycles, single-end) system.

540 Analysis of CMS-IP data was performed by in-house software 'CMSIP' v0.1.1
541 (https://github.com/lijinbio/cmsip). Briefly, raw reads were mapped to hg38 and mm10 genome
542 references using bsmap v.2.89 [59] (options: -n 1 -q 3 -r 0). After removing PCR duplicates and reads
543 mapped to both human and spike-in mouse genome, species-specific reads were used to perform
544 normalization for each sample according to the spike-in size factors. The mean wigsum for every
545 200-bp window of the whole human genome was used to call the hydroxymethylation-enriched peak
546 regions for each group against input. In total, 75,324 and 503 peaks were detected in WT_PP and
547 TKO_PP samples, respectively. Differentially DHMRs between WT_PP and TKO_PP were
548 identified (g-test; FDR < 0.05). GREAT analysis with single-nearest genes option was used to
549 perform functional annotation of hypo-DHMRs.

550 CMS-IP-seq datasets of hESCs and multiple pancreatic lineage intermediates (DE, GT, and PP)
551 were downloaded from GSE97992 [21] and mapped to the hg38 reference genome using bsmap with
552 the same parameters as in the previous analysis. Bam2wig.py in RSeQC [60] was used to transform the
553 bam file to normalized bigWig files (option: -t 2000000000). The average 5hmC signals within each
554 hypo-DHMR for all stages were calculated using deepTools [61]. Compared with hESCs, increased
555 5hmC peaks were defined as peaks in PP cells with a ≥ 1.5-fold increase.

556 **WGBS library preparation and data analysis**. Genomic DNA was isolated using the DNeasy
557 Blood & Tissue kit (Qiagen). Library preparation and high-throughput sequencing were conducted
558 by BGI (Shengzhen, China). In brief, purified genomic DNA (with 1% unmethylated lambda DNA
559 spike-in, Promega) was sheared to a fragment size of 100–700 bp (primary size 250 bp). Sheared
560 DNA was ligated with methylated adaptors (MGIEasy WGBS Adapters-16, MGI) and subjected to
561 bisulfite conversion using the EZ DNA Methylation-gold kit (Zymo Research). Bisulfite-converted
562 DNA was amplified with 13 PCR cycles and purified by AMPure XP beads (Beckman Coulter). All
563 libraries were sequenced on an MGISEQ-2000 system (100-cycle, paired-end).

564 For data analysis, paired-end 100 bp reads were mapped against hg38 using bsmap v.2.89 [59] with
565 paired mode (options: -n 1 -q 3 -r 0), and only uniquely mapped reads were retained. More than 26.6
566 million CpG sites with coverage of ≥ 5 reads were detected in both WT_PP and TKO_PP samples,
567 which were used for downstream analyses. BSeQC [62] and the mcall module in MOABS [29] was applied
568 to perform quality control and calculate the methylation ratio for each CpG site (options: --
569 trimWGBSEndRepairPE2Seq 40). Bisulfite conversion efficiencies were estimated using spike-in
570 unmethylated lambda phage DNA. The Mcomp module was used to call significant DMCs and DMRs
571 (absolute credible difference of DNA methylation ratio > 20% and adjusted $p < 0.05$). The output
572 bedGraph files from mcall included single-base resolution DNA methylation ratios, which were
573 transformed into bigwig file format. The bigwig files were uploaded to the UCSC genome browser
574 for visualization. Motif enrichment analysis of DMRs was performed using HOMER software,
575 functional annotation was performed using GREAT [20] with default settings, and many plots related
576 to WGBS was performed using MMINT.

577 **ChIP-seq library preparation and data analysis**. ChIP-seq was performed for TET1 (WT_PP cells),
578 H3K4me1 (WT_PP and TKO_PP cells), and H3K27ac (WT_PP and TKO_PP cells). For TET1 ChIP-
579 seq, ~5 × 10^7 cells were crosslinked, washed, and snap-frozen following the Cell Fixation protocol
580 from Active Motif. TET1 ChIP-seq library preparation and sequencing were conducted by Active
581 Motif. Chromatin immunoprecipitation of H3K4me1 and H3K27ac were performed as previously
582 described [28]. WT_PP and TKO_PP cells were fixed, washed, and lysed in nuclear lysis buffer (50
583 mM Trish HCl, pH 8.0, 5 mM EDTA, 1% SDS, and 1× protease inhibitor cocktail). Chromatin was
584 sheared to 200–500-bp fragments using Bioruptor (Diagenode), and DNA fragments were
585 precipitated with appropriate antibodies. ChIP-seq libraries were prepared using the NEBNext Ultra
586 II DNA Library Prep kit (New England Biolabs) following the manufacturer's instruction and
587 subjected to high-throughput sequencing on an Illumina HiSeq 2500 system (150 bp, paired-end) at
588 Novogene (Tianjin, China).

589 Quality control and alignment of raw reads of ChIP-seq data were performed similarly to the
590 ATAC-seq data analysis described above. TrimGalore (options: --quality 20 and --length 50) was
591 used to remove the adaptor, and only uniquely mapped reads were retained. Bam2wig.py was used
592 to transform the bam file to normalized bigWig files (option: -t 2000000000). For WT_PP TET1
593 ChIP-seq, Macs2 [63] was used to call ChIP-seq enriched peak regions with default parameters.

594 **Integration of analyses**. RNA-seq, WGBS, CMS-IP-seq, ATAC-seq and ChIP-seq library
595 preparations were performed as previously described. Detail experimental procedures can be found
596 in Supplementary Materials. The number of mapped reads and mapped ratios are listed in
597 Supplementary Table 8. To compare 5hmC and FOXA2 enriched signals, FOXA2 ChIP-seq datasets
598 of multiple pancreatic lineage intermediates were downloaded from GSE117136. Data were analyzed

599 as described above. Deeptools was used to calculate average signals at pancreas-specific hypo-
600 DHMRs (up- and down- 3 kb) in each group. The FOXA2 bound sites were detected using Macs2 [63].

601 To compare DNA methylation between TKO_PP and WT_PP cells at annotated genomic
602 features, ChIP-seq datasets of FOXA2, GATA4, GATA6, and PDX1 were downloaded from
603 GSE117136. Bivalent promoters and poised and active enhancers in hESC-derived pancreatic
604 progenitors were downloaded from EMTAB1086 and GSE54471, respectively. The analysis was
605 similar to that described above.

606 **Quantification and statistical analysis**. All statistical analyses were performed using GraphPad
607 Prism software. Student's unpaired two-tailed *t*-tests were used for qRT-PCR and flow cytometry
608 experiments. Student's paired one-tailed *t*-tests were used for the glucose-stimulated human C-
609 peptide secretion experiment. Quantification data are presented as mean ± SD. For all statistical
610 analyses, $*p < 0.05$, $**p < 0.01$, $***p < 0.001$, and $****p < 0.0001$. Statistical analyses for RNA-seq,
611 WGBS, CMS-IP-seq, and ChIP-seq data are described in the corresponding sections.

612

613 **Data availability**

614 WGBS, CMS-IP, RNA-seq, ATAC-seq, and ChIP-seq data from this study were submitted to the
615 NCBI Gene Expression Omnibus (GEO; https://www.ncbi.nlm.nih.gov/geo/) under accession
616 number GSE146486. All relevant data supporting the critical findings of this study are available
617 within the article and its supplementary information files or from the corresponding author upon
618 reasonable request.

619

620 **Acknowledgments**

621 We thank the University of Macau, Faculty of Health Sciences, Animal Research Facility for
622 animal housing. This work was supported by the National Natural Science Foundation of China
623 (NSFC 31701276) and the University of Macau Multi-Year Research Grant (MYRG2016-00065-
624 FHS) to R.X.

625

626 **Author contributions**

627 R.X. conceived the project. R.X. and D.S. directed and oversaw the project. X.W. performed most
628 experiments and collected data. J.F.L. performed computational analysis for WGBS, RNA-seq, CMS-
629 IP-seq, ATAC-seq, and ChIP-seq. M.L. prepared the CMS-IP library and performed sequencing. Q.L.
630 assisted with the animal studies. J.L. provided expert advice on bioinformatic analyses. Y.H. critically
631 reviewed the manuscript. R.X., X.W., D.S., and J.F.L. wrote the manuscript; all other authors
632 provided editorial advice.

633

634 **Competing interests**

635 The authors declare that no conflicts of interest exist.

636 **References**

637 1. Buecker, C. & Wysocka, J. Enhancers as information integration hubs in development: lessons
638 from genomics. *Trends Genet.* **28**, 276-284 (2012).
639 2. Long, H. K., Prescott, S. L. & Wysocka, J. Ever-changing landscapes: transcriptional
640 enhancers in development and evolution. *Cell* **167**, 1170-1187 (2016).
641 3. Wang, A. et al. Epigenetic priming of enhancers predicts developmental competence of hESC-
642 derived endodermal lineage intermediates. *Cell Stem Cell* **16**, 386-399 (2015).
643 4. Lee, K. et al. FOXA2 is required for enhancer priming during pancreatic differentiation. *Cell*
644 *Rep* **28**, 382-393 (2019).
645 5. Cirillo, L. A. & Zaret, K. S. An early developmental transcription factor complex that is more
646 stable on nucleosome core particles than on free DNA. *Mol. Cell* **4**, 961-969 (1999).
647 6. Cirillo, L. A. et al. Opening of compacted chromatin by early developmental transcription
648 factors HNF3 (FoxA) and GATA-4. *Mol. Cell* **9**, 279-289 (2002).
649 7. Iwafuchi-Doi, M. et al. The pioneer transcription factor foxA maintains an accessible
650 nucleosome configuration at enhancers for tissue-specific gene activation. *Mol. Cell* **62**, 79-
651 91 (2016).
652 8. Serandour, A. A. et al. Epigenetic switch involved in activation of pioneer factor FOXA1-
653 dependent enhancers. *Genome Res.* **21**, 555-565 (2011).
654 9. Donaghey, J. et al. Genetic determinants and epigenetic effects of pioneer-factor occupancy.
655 *Nat. Genet.* **50**, 250-258 (2018).
656 10. He, Y. F. et al. Tet-mediated formation of 5-carboxylcytosine and its excision by TDG in
657 mammalian DNA. *Science* **333**, 1303-1307 (2011).
658 11. Ito, S. et al. Role of Tet proteins in 5mC to 5hmC conversion, ES-cell self-renewal and inner
659 cell mass specification. *Nature* **466**, 1129-1133 (2010).
660 12. Ito, S. et al. Tet proteins can convert 5-methylcytosine to 5-formylcytosine and 5-
661 carboxylcytosine. *Science* **333**, 1300-1303 (2011).
662 13. Tahiliani, M. et al. Conversion of 5-methylcytosine to 5-hydroxymethylcytosine in
663 mammalian DNA by MLL partner TET1. *Science* **324**, 930-935 (2009).
664 14. Zhang, H. et al. TET1 is a DNA-binding protein that modulates DNA methylation and gene
665 transcription via hydroxylation of 5-methylcytosine. *Cell Res.* **20**, 1390-1393 (2010).
666 15. Tsagaratou, A. et al. Dissecting the dynamic changes of 5-hydroxymethylcytosine in T-cell
667 development and differentiation. *Proc. Natl. Acad. Sci. USA* **111**, E3306-3315 (2014).
668 16. Tan, L. et al. Genome-wide comparison of DNA hydroxymethylation in mouse embryonic
669 stem cells and neural progenitor cells by a new comparative hMeDIP-seq method. *Nucleic*
670 *Acids Res.* **41**, e84 (2013).
671 17. Kim, M. et al. Dynamic changes in DNA methylation and hydroxymethylation when hES
672 cells undergo differentiation toward a neuronal lineage. *Hum. Mol. Genet.* **23**, 657-667 (2014).
673 18. Verma, N. et al. TET proteins safeguard bivalent promoters from de novo methylation in
674 human embryonic stem cells. *Nat. Genet.* **50**, 83-95 (2018).
675 19. Ko, M. et al. Ten-Eleven-Translocation 2 (TET2) negatively regulates homeostasis and
676 differentiation of hematopoietic stem cells in mice. *Proc. Natl. Acad. Sci. USA* **108**, 14566-

677 14571 (2011).
678 20. Fang, S. et al. Tet inactivation disrupts YY1 binding and long-range chromatin interactions
679 during embryonic heart development. *Nat. Commun.* **10**, 4297 (2019).
680 21. Li, J. et al. Decoding the dynamic DNA methylation and hydroxymethylation landscapes in
681 endodermal lineage intermediates during pancreatic differentiation of hESC. *Nucleic Acids*
682 *Res.* **46**, 2883-2900 (2018).
683 22. Lu, F. L., Liu, Y. T., Jiang, L., Yamaguchi, S. & Zhang, Y. Role of Tet proteins in enhancer
684 activity and telomere elongation. *Genes Dev.* **28**, 2103-2119 (2014).
685 23. Rodriguez-Segui, S., Akerman, I. & Ferrer, J. GATA believe it: new essential regulators of
686 pancreas development. *J. Clin. Invest.* **122**, 3469-3471 (2012).
687 24. Kaestner, K. H. The FoxA factors in organogenesis and differentiation. *Curr. Opin. Genet.*
688 *Dev.* **20**, 527-532 (2010).
689 25. Zhang, H. et al. Multiple, temporal-specific roles for HNF6 in pancreatic endocrine and ductal
690 differentiation. *Mech. Dev.* **126**, 958-973 (2009).
691 26. Lopez-Moyado, I. F. et al. Paradoxical association of TET loss of function with genome-wide
692 DNA hypomethylation. *Proc. Natl. Acad. Sci. USA* **116**, 16933-16942 (2019).
693 27. Walsh, C. P., Chaillet, J. R. & Bestor, T. H. Transcription of IAP endogenous retroviruses is
694 constrained by cytosine methylation. *Nat. Genet.* **20**, 116-117 (1998).
695 28. Xie, R. et al. Dynamic chromatin remodeling mediated by polycomb proteins orchestrates
696 pancreatic differentiation of human embryonic stem cells. *Cell Stem Cell* **12**, 224-237 (2013).
697 29. Sun, D. et al. MOABS: model based analysis of bisulfite sequencing data. *Genome Biol.* **15**,
698 R38 (2014).
699 30. Consortium, E. P. An integrated encyclopedia of DNA elements in the human genome. *Nature*
700 **489**, 57-74 (2012).
701 31. Volkov, P. et al. Whole-genome bisulfite sequencing of human pancreatic islets reveals novel
702 differentially methylated regions in type 2 diabetes pathogenesis. *Diabetes* **66**, 1074-1085
703 (2017).
704 32. Akerman, I. et al. Human pancreatic beta cell lncRNAs control cell-specific regulatory
705 networks. *Cell Metab.* **25**, 400-411 (2017).
706 33. Sosa-Pineda, B., Chowdhury, K., Torres, M., Oliver, G. & Gruss, P. The Pax4 gene is essential
707 for differentiation of insulin-producing beta cells in the mammalian pancreas. *Nature* **386**,
708 399-402 (1997).
709 34. Nelson, S. B., Schaffer, A. E. & Sander, M. The transcription factors Nkx6.1 and Nkx6.2
710 possess equivalent activities in promoting beta-cell fate specification in Pdx1+ pancreatic
711 progenitor cells. *Development* **134**, 2491-2500 (2007).
712 35. Ohta, Y. et al. Convergence of the insulin and serotonin programs in the pancreatic beta-cell.
713 *Diabetes* **60**, 3208-3216 (2011).
714 36. Wu, H. et al. Dual functions of Tet1 in transcriptional regulation in mouse embryonic stem
715 cells. *Nature* **473**, 389-393 (2011).
716 37. Cernilogar, F. M. et al. Pre-marked chromatin and transcription factor co-binding shape the
717 pioneering activity of Foxa2. *Nucleic Acids Res.* **47**, 9069-9086 (2019).
718 38. Ahlgren, U., Jonsson, J., Jonsson, L., Simu, K. & Edlund, H. Beta-cell-specific inactivation

of the mouse Ipf1/Pdx1 gene results in loss of the beta-cell phenotype and maturity onset diabetes. *Genes Dev.* **12**, 1763-1768 (1998).

39. Sussel, L. et al. Mice lacking the homeodomain transcription factor Nkx2.2 have diabetes due to arrested differentiation of pancreatic beta cells. *Development* **125**, 2213-2221 (1998).
40. Collombat, P. et al. Opposing actions of Arx and Pax4 in endocrine pancreas development. *Genes Dev.* **17**, 2591-2603 (2003).
41. Dhawan, S., Georgia, S., Tschen, S. I., Fan, G. & Bhushan, A. Pancreatic beta cell identity is maintained by DNA methylation-mediated repression of Arx. *Dev. Cell* **20**, 419-429 (2011).
42. Liu, J. et al. Neurog3-independent methylation is the earliest detectable mark distinguishing pancreatic progenitor identity. *Dev. Cell* **48**, 49-63 (2019).
43. Papizan, J. B. et al. Nkx2.2 repressor complex regulates islet beta-cell specification and prevents beta-to-alpha-cell reprogramming. *Genes Dev.* **25**, 2291-2305 (2011).
44. Wu, X., Li, G. & Xie, R. Decoding the role of TET family dioxygenases in lineage specification. *Epigenetics Chromatin* **11**, 58 (2018).
45. Serandour, A. A. et al. Dynamic hydroxymethylation of deoxyribonucleic acid marks differentiation-associated enhancers. *Nucleic Acids Res* **40**, 8255-8265 (2012).
46. Yang, Y. A. et al. FOXA1 potentiates lineage-specific enhancer activation through modulating TET1 expression and function. *Nucleic Acids Res.* **44**, 8153-8164 (2016).
47. Lio, C. W. et al. Tet2 and Tet3 cooperate with B-lineage transcription factors to regulate DNA modification and chromatin accessibility. *Elife* **5**, e18290 (2016).
48. Rezania, A. et al. Reversal of diabetes with insulin-producing cells derived in vitro from human pluripotent stem cells. *Nat. Biotechnol.* **32**, 1121-1133 (2014).
49. Zmuda, E. J., Powell, C. A. & Hai, T. A method for murine islet isolation and subcapsular kidney transplantation. *J. Vis. Exp.* **50**, 2096 (2011).
50. Cong, L. et al. Multiplex genome engineering using CRISPR/Cas systems. *Science* **339**, 819-823 (2013).
51. Tu, S. et al. Takusan: a large gene family that regulates synaptic activity. *Neuron* **55**, 69-85 (2007).
52. Dobin, A. et al. STAR: ultrafast universal RNA-seq aligner. *Bioinformatics* **29**, 15-21 (2013).
53. Anders, S., Pyl, P. T. & Huber, W. HTSeq--a Python framework to work with high-throughput sequencing data. *Bioinformatics* **31**, 166-169 (2015).
54. Love, M. I., Huber, W. & Anders, S. Moderated estimation of fold change and dispersion for RNA-seq data with DESeq2. *Genome Biol.* **15**, 550 (2014).
55. Gu, Z., Eils, R. & Schlesner, M. Complex heatmaps reveal patterns and correlations in multidimensional genomic data. *Bioinformatics* **32**, 2847-2849 (2016).
56. Yu, G., Wang, L. G., Han, Y. & He, Q. Y. ClusterProfiler: an R package for comparing biological themes among gene clusters. *OMICS* **16**, 284-287 (2012).
57. Buenrostro, J. D., Wu, B., Chang, H. Y. & Greenleaf, W. J. ATAC-seq: a method for assaying chromatin accessibility genome-wide. *Curr. Protoc. Mol. Biol.* **109**, 21.29.21-21.29.29 (2015).
58. Heinz, S. et al. Simple combinations of lineage-determining transcription factors prime cis-regulatory elements required for macrophage and B cell identities. *Mol. Cell* **38**, 576-589 (2010).

59. Cowley, M. et al. Effects of cadmium exposure on DNA methylation at imprinting control regions and genome-wide in mothers and newborn children. *Environ. Health Perspect.* **126**, 037003 (2018).
60. Wang, L., Wang, S. & Li, W. RSeQC: quality control of RNA-seq experiments. *Bioinformatics* **28**, 2184-2185 (2012).
61. Ramirez, F., Dundar, F., Diehl, S., Gruning, B. A. & Manke, T. DeepTools: a flexible platform for exploring deep-sequencing data. *Nucleic Acids Res.* **42**, W187-191 (2014).
62. Lin, X. et al. BSeQC: quality control of bisulfite sequencing experiments. *Bioinformatics* **29**, 3227-3229 (2013).
63. Feng, J., Liu, T., Qin, B., Zhang, Y. & Liu, X. S. Identifying ChIP-seq enrichment using MACS. *Nat. Protoc.* **7**, 1728-1740 (2012).

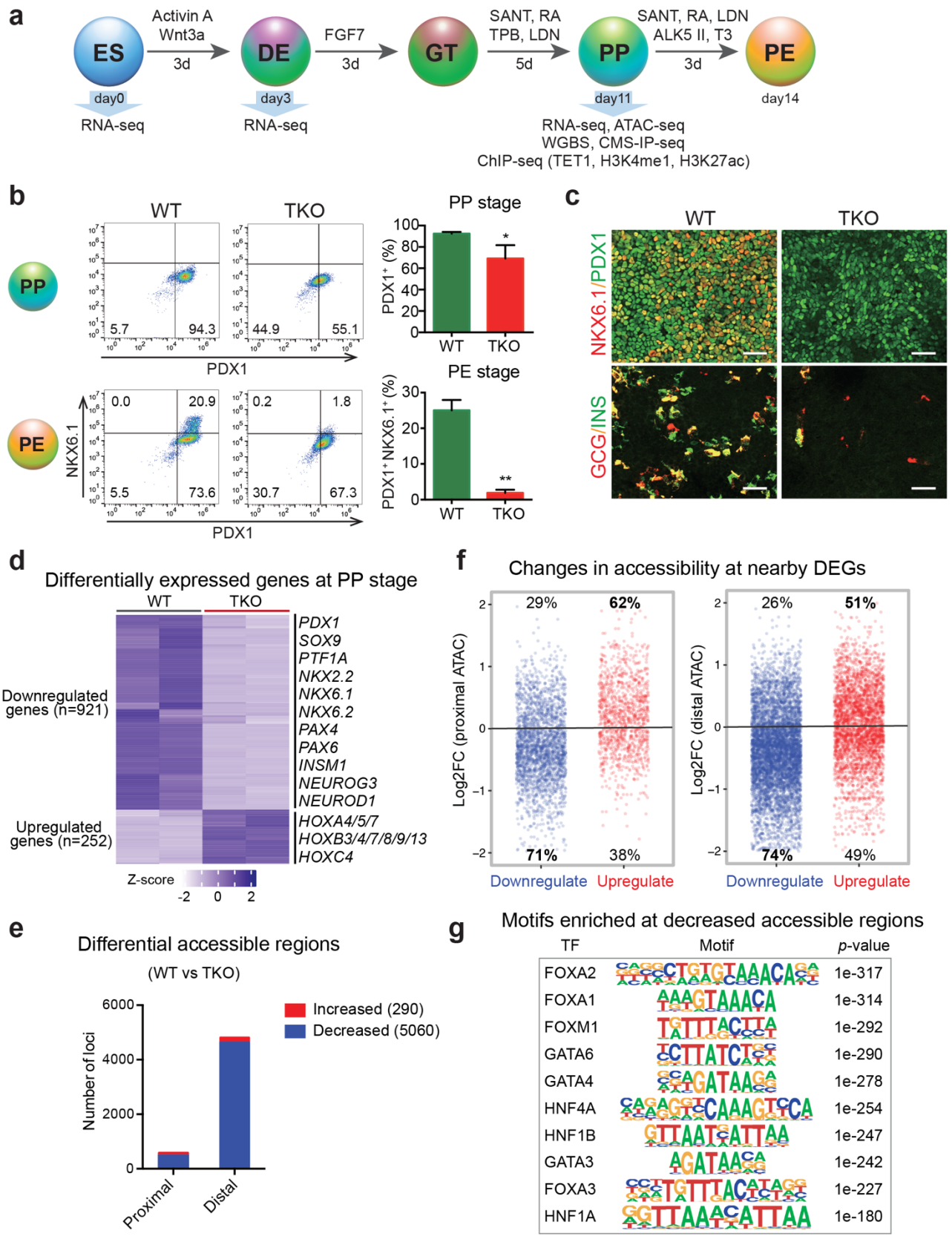
a
ES
Activin A
Wnt3a
3d
DE
FGF7
3d
GT
SANT, RA
TPB, LDN
5d
PP
SANT, RA, LDN
ALK5 II, T3
3d
PE
day0
RNA-seq
day3
RNA-seq
day11
RNA-seq, ATAC-seq
WGBS, CMS-IP-seq
ChIP-seq (TET1, H3K4me1, H3K27ac)
day14
b
WT
TKO
PP
PE
PDX1
NKX6.1
5.7
94.3
44.9
55.1
0.0
20.9
0.2
1.8
5.5
73.6
30.7
67.3
PP stage
PE stage
PDX1+ (%)
PDX1+NKX6.1+ (%)
c
NKX6.1/PDX1
GCG/INS
d
Differentially expressed genes at PP stage
Downregulated genes (n=921)
Upregulated genes (n=252)
PDX1
SOX9
PTF1A
NKX2.2
NKX6.1
NKX6.2
PAX4
PAX6
INSM1
NEUROG3
NEUROD1
HOXA4/5/7
HOXB3/4/7/8/9/13
HOXC4
Z-score
e
Differential accessible regions
(WT vs TKO)
Increased (290)
Decreased (5060)
Number of loci
Proximal
Distal
f
Changes in accessibility at nearby DEGs
Log2FC (proximal ATAC)
Log2FC (distal ATAC)
29%
62%
71%
38%
26%
51%
74%
49%
Downregulate
Upregulate
g
Motifs enriched at decreased accessible regions
TF
Motif
p-value
FOXA2
1e-317
FOXA1
1e-314
FOXM1
1e-292
GATA6
1e-290
GATA4
1e-278
HNF4A
1e-254
HNF1B
1e-247
GATA3
1e-242
FOXA3
1e-227
HNF1A
1e-180

773

774 **Fig. 1 TET hydroxylases are required for pancreatic endocrine lineage specification.**

775 **a** Stepwise differentiation of hESCs to pancreatic endocrine cells. Wild-type (WT) and
776 *TET1*/*TET2*/*TET3* triple knock-out (TKO) hESC lines were differentiated and analyzed by RNA-seq,
777 WGBS, CMS-IP-seq, ATAC-seq, and ChIP-seq at the indicated stages (ES: embryonic stem cell; DE:
778 definitive endoderm; GT: primitive gut tube; PP: pancreatic progenitor; PE: pancreatic endocrine). **b**
779 Representative flow cytometry plots for PDX1 and NKX6.1 in WT or TKO cells at the PP and PE
780 stages. Quantification of the percentage of $PDX1^+$ $NKX6.1^+$ cells is shown in the right panel. n = 3
781 independent differentiation. **c** Immunostaining of PDX1/NKX6.1 at the PP stage and insulin
782 (INS)/glucagon (GCG) at the PE stage are shown in WT and TKO cells. Scale bar = 50 μm. **d** Genes
783 with significant changes in expression in TKO cells relative to WT cells at the PP stage. Differentially
784 expressed genes (DEGs) are classified into down- and upregulated groups. Each row corresponds to
785 one individual gene and each column to a different biological repeat. The color scale from white to
786 blue represents Z-score normalized gene expression levels from low to high (FDR < 0.05). **e** Number
787 of regions with significant changes in chromatin accessibility upon TET depletion at proximal (≤ 1
788 kb from TSS) and distal (> 1 kb from TSS) regions ($p < 0.05$). **f** Dot plots depicting the ratios (WT_PP
789 over TKO_PP) of ATAC signals (y-axis) at proximal (left) or distal (right) regions of DEGs that were
790 downregulated (blue) or upregulated (red) in TKO_PP cells compared with WT_PP cells. Values
791 indicate the fraction of increased or decreased chromatin accessibility regions in down- and
792 upregulated genes, respectively. **g** Transcription factor (TF) motif enrichment analysis of genomic
793 regions showed significantly decreased ATAC-seq signals in TKO_PP cells. The top 10 significant
794 motifs are shown after removing redundant motifs.

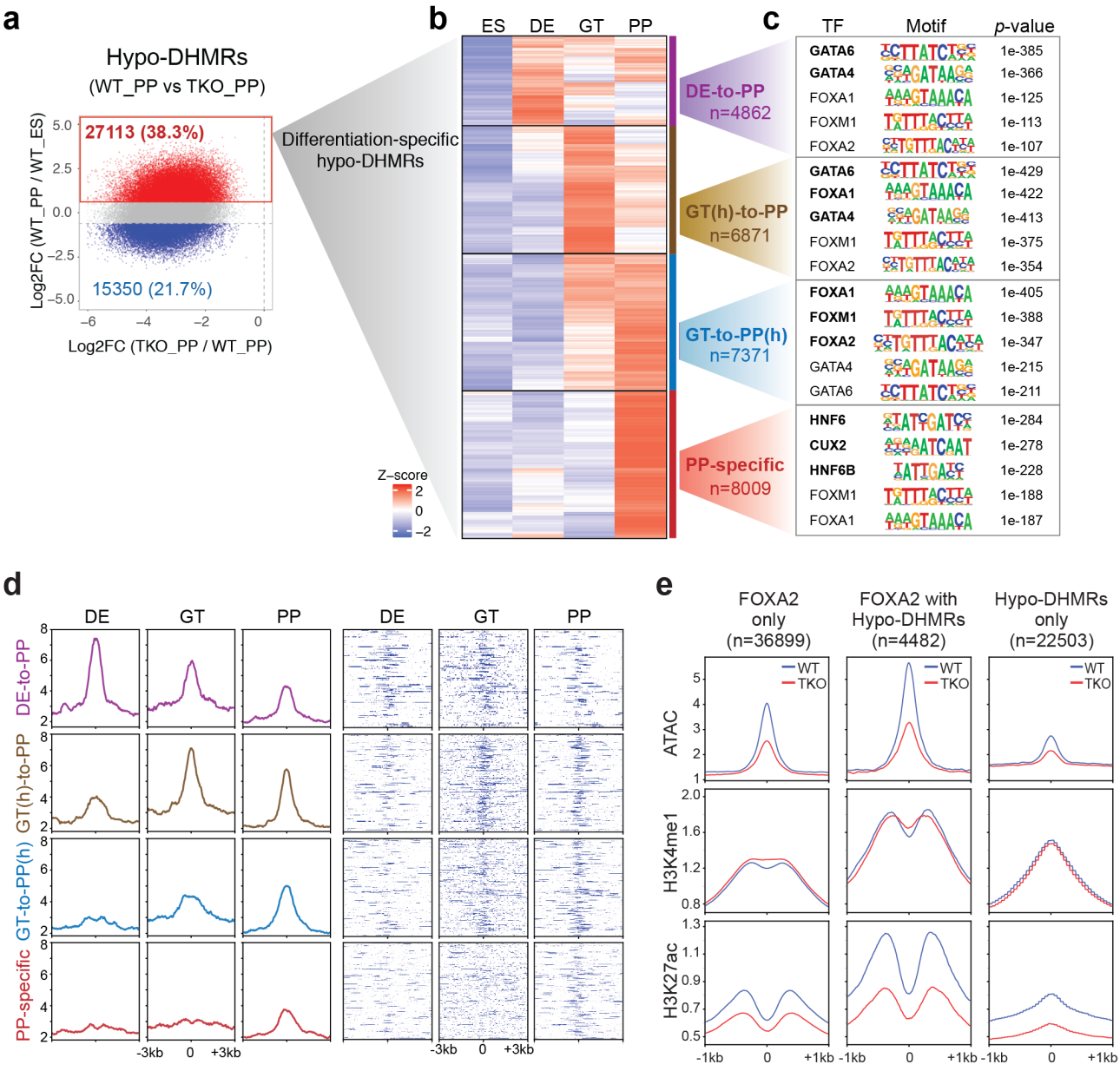

Fig. 2 Loss of TET disrupts epigenetic dynamics at pancreas-specific hypo-DHMRs associated with distinct pioneer TFs motifs.

a Scatterplot presenting 5hmC differences between pancreatic progenitors (WT_PP) and hESCs (WT_ES) at hypo-DHMRs identified in TKO_PP cells. Red indicates increased 5hmC (fold change > 1.5), and blue shows decreased 5hmC in pancreatic progenitors relative to hESCs. **b** Clustering of 5hmC signals in WT cells at four differentiation stages (ES, DE, GT, and PP). Each row represents one hypo-DHMR showing increased 5hmC in pancreatic progenitors compared with hESCs. Red

803 represents high 5hmC; blue indicates low 5hmC. **c** Motif enrichment analysis among the four clusters
804 defined in **b**. The top five known motifs are shown. **d** Heatmap and density plots showing dynamic
805 changes of FOXA2 in the DE, GT, and PP lineage intermediates across the four clusters defined in **b**.
806 The color scale from white to blue represents normalized FOXA2 signal from low to high. **e**
807 Enrichment profile of chromatin accessibility (ATAC), H3K4me1, and H3K27ac at regions of
808 FOXA2 binding alone (left column), FOXA2 binding together with 'differentiation-specific hypo-
809 DHMRs' (middle column), and 'differentiation-specific hypo-DHMRs' alone (right column). The
810 WT signal is marked in blue and the TKO signal in red.

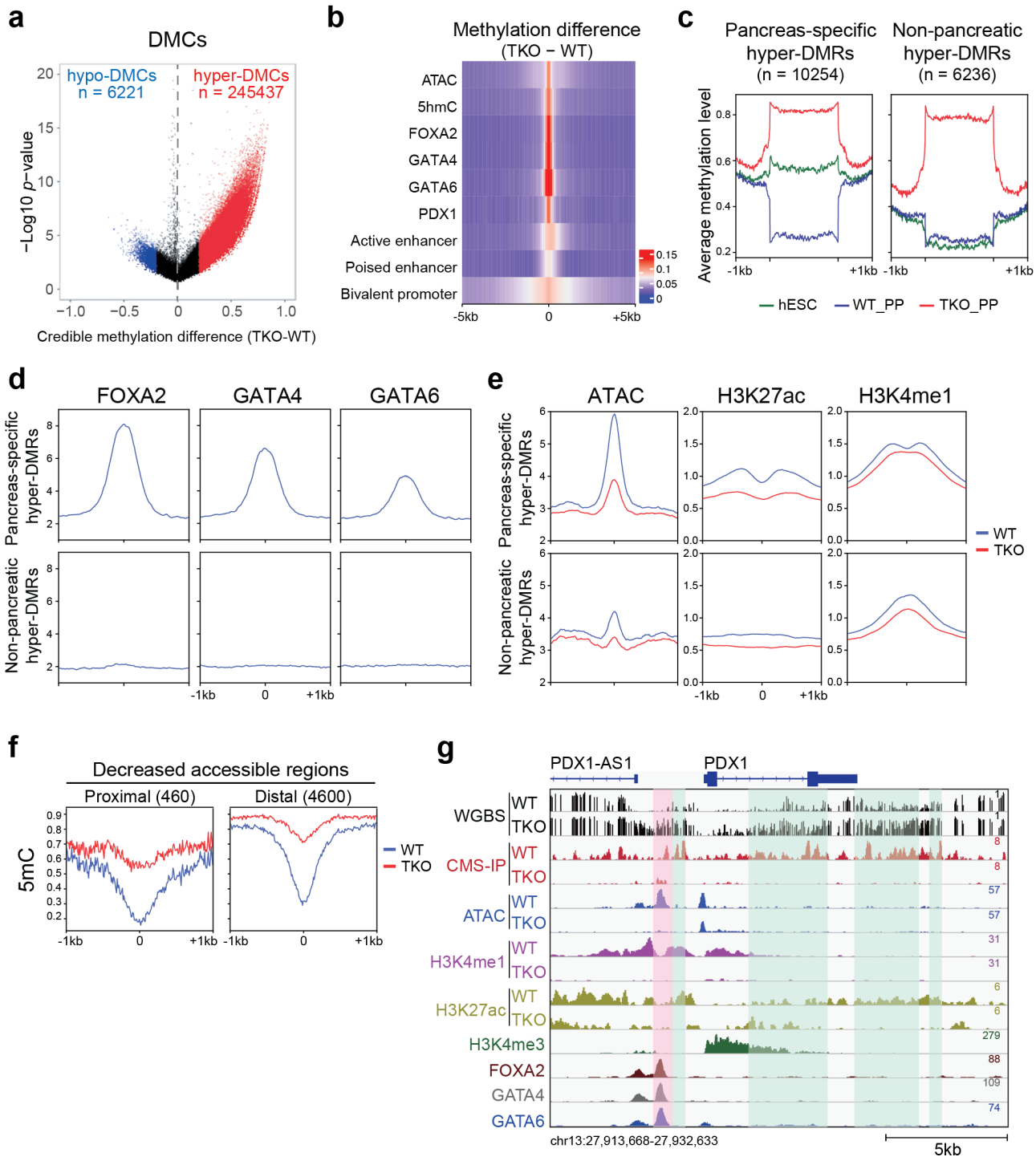
a
DMCs
hypo-DMCs
n = 6221
hyper-DMCs
n = 245437
−Log10 p−value
Credible methylation difference (TKO-WT)
b
Methylation difference
(TKO − WT)
ATAC
5hmC
FOXA2
GATA4
GATA6
PDX1
Active enhancer
Poised enhancer
Bivalent promoter
-5kb
0
+5kb
c
Pancreas-specific
hyper-DMRs
(n = 10254)
Non-pancreatic
hyper-DMRs
(n = 6236)
Average methylation level
-1kb
+1kb
hESC
WT_PP
TKO_PP
d
FOXA2
GATA4
GATA6
Pancreas-specific
hyper-DMRs
Non-pancreatic
hyper-DMRs
e
ATAC
H3K27ac
H3K4me1
WT
TKO
f
Decreased accessible regions
Proximal (460)
Distal (4600)
5mC
g
PDX1-AS1
PDX1
WGBS
CMS-IP
ATAC
H3K4me1
H3K27ac
H3K4me3
FOXA2
GATA4
GATA6
chr13:27,913,668-27,932,633
5kb

811

812 **Fig. 3 Pancreas-specific hyper-DMRs show reduced chromatin activity during pancreatic**

813 **differentiation.**

814 **a** Volcano plot of WGBS data illustrating differentially methylated CpGs (DMCs) identified in

815 TKO_PP cells compared with WT_PP cells. Red and blue represent increased and decreased 5mC in

816 TKO_PP cells, respectively (credible methylation difference > 0.2). **b** Heatmap illustrating

817 methylation difference between TKO_PP and WT_PP cells at centers of annotated genomic features

818 (± 5 kb) for chromatin accessibility (ATAC), hydroxylation (5hmC), TF binding (FOXA2, GATA4,

819 GATA6, and PDX1), bivalent promoters, poised enhancers, and active enhancers. Average 5mC

820 signals of every 100-bp bin were calculated. **c** Classification of TKO hyper-DMRs based on 5mC

821 levels in hESCs (green), WT_PP cells (blue), and TKO_PP cells (red). **d** Average plots of FOXA2

822 (left column), GATA4 (middle column), and GATA6 (right column) signal at pancreas-specific

823 hyper-DMRs or non-pancreatic hyper-DMRs in pancreatic progenitors. **e** Average plots of ATAC

824 (left column), H3K27ac (middle column), and H3K4me1 (right column) at pancreas-specific hyper-

825 DMRs or non-pancreatic hyper-DMRs in WT_PP (blue) and TKO_PP (red) cells. **f** Average plots of

826 5mC at proximal (≤ 1 kb from TSS) and distal (> 1 kb from TSS) decreased accessible regions in

827 WT_PP (blue) and TKO_PP (red) cells. **g** Genome-browser view of the *PDX1/PDX1-AS1* locus. Four

828 type 2 diabetes-associated islet hyper-DMRs [31] overlapping with TKO hyper-DMRs are highlighted

829 in green. A specific TKO hyper-DMR showing decreased ATAC, H3K4me1, and H3K27ac signals

830 is highlighted in pink.

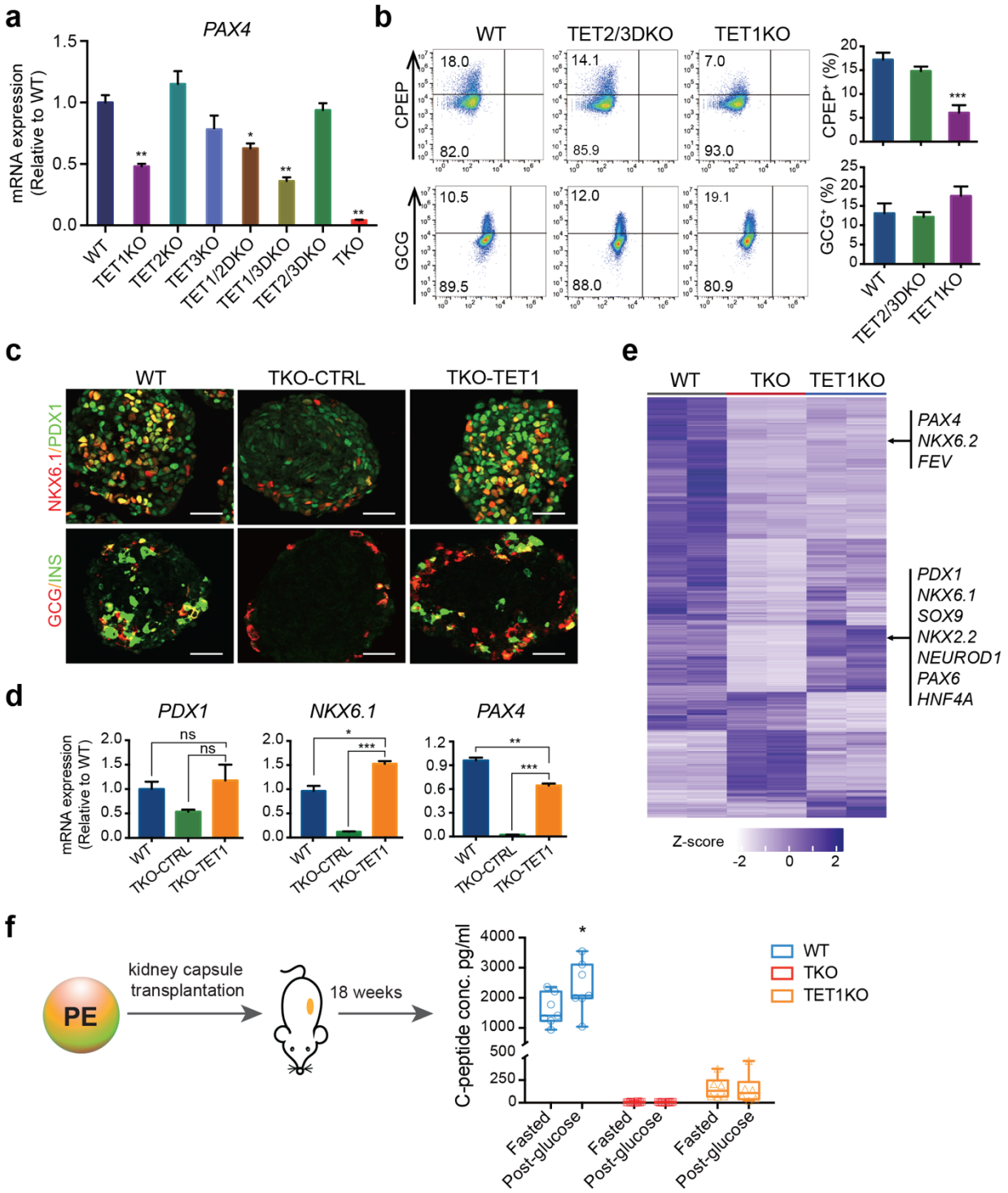

Fig. 4 TET1 is required in pancreatic β-cell specification.

a Expression of *PAX4* in WT, TET1KO, TET2KO, TET3KO, TET1/2DKO, TET1/3DKO, TET2/3DKO, and TKO cells at the PP stage by RT-qPCR. RT-qPCR validation was performed with three independent batches of samples. **b** Representative plots of flow cytometry of human C-peptide

836 (CPEP) and glucagon (GCG) in WT, TET1KO, and TET2/3DKO cells at the PE stage.
837 Quantifications of the percentage of $CPEP^+$ or GCG^+ cells are shown in the right panel. n = 3
838 independent differentiation. **c** Immunostaining of NKX6.1, PDX1, INS, and GCG in WT, TKO-
839 CTRL, and TKO-TET1 cells at the PE stage of pancreatic differentiation. Scale bar = 50 μm. **d**
840 Expression of *PDX1*, *NKX6.1*, and *PAX4* in WT, TKO-CTRL, and TKO-TET1 cells at the PP stage
841 by RT-qPCR. RT-qPCR validation was performed with three independent batches of samples. **e**
842 Heatmap showing the hierarchical clustering of DEGs among WT_PP, TKO_PP, and TET1KO_PP
843 cells. Each row represents one DEG, and each column represents one biological replicate. The color
844 scale from white to blue represents normalized gene expression levels from low to high (FDR < 0.05).
845 **f** WT, TKO, and TET1KO cells were differentiated to the PE stage and transplanted under the kidney
846 capsule of nondiabetic female SCID-beige mice. Eighteen weeks post-implantation, human C-peptide
847 levels were measured after an overnight fast and 30 min following an i.p. glucose injection. C-peptide
848 levels from individual mice are shown in box and whisker plots.

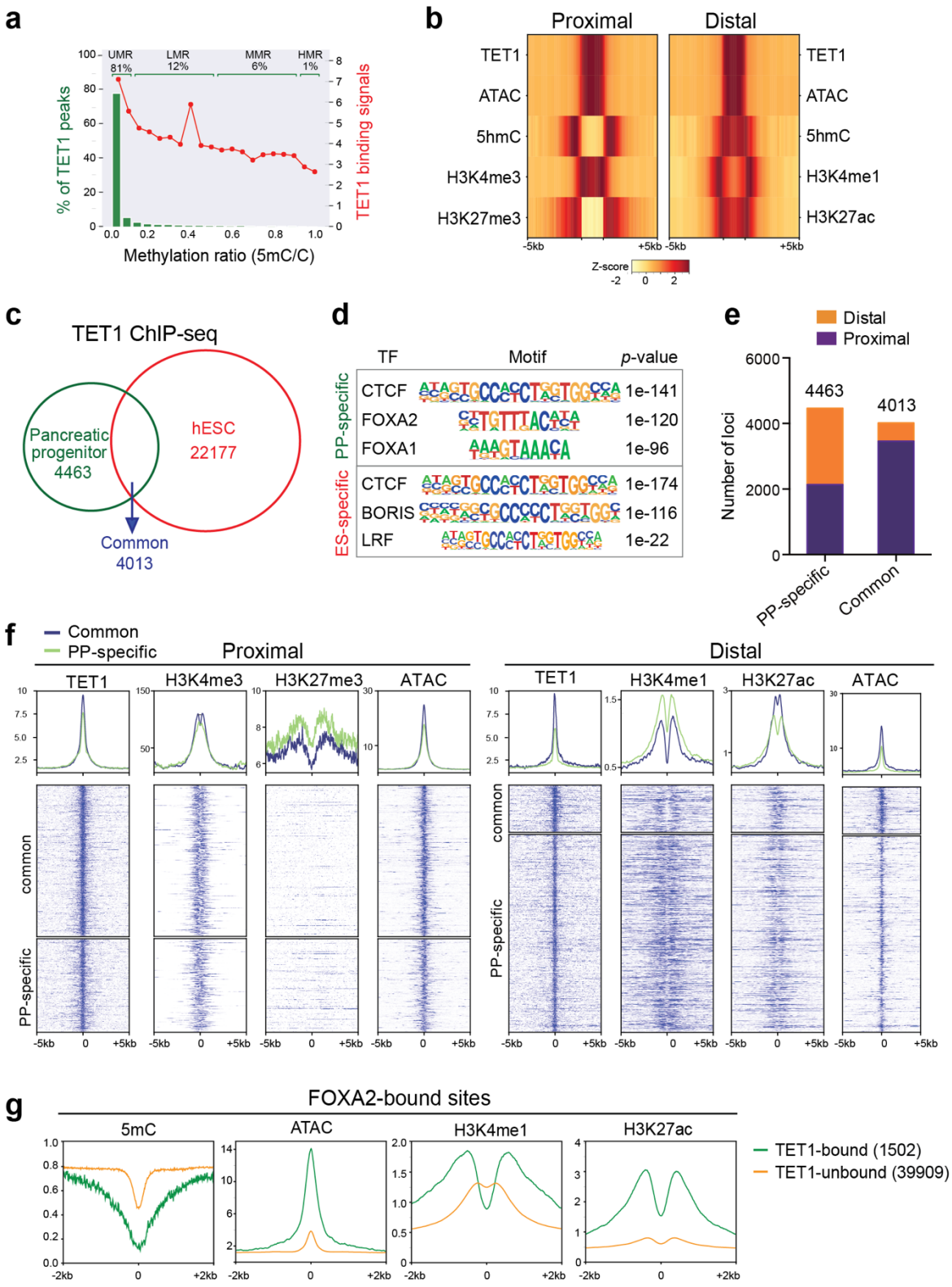

Fig. 5 TET1 binding sites are distinct in pancreatic progenitors.

a Methylation levels at TET1 binding sites in WT_PP cells. The x-axis represents the average methylation ratio of CpG sites located within each peak (at 5% methylation ratio intervals). The green

853 bar represents the percentage of TET1 peaks within the corresponding methylation ratio interval (left
854 y-axis). The red curve indicates TET1-enriched signals within each corresponding methylation ratio
855 interval (right y-axis). The numerical labels at the top represent the fraction of the four class peaks
856 with different average methylation ratios: UMR, unmethylated regions (0-0.1); LMR, low methylated
857 regions (0.1-0.5); MMR, medium methylated regions (0.5-0.9); and HMR, high methylated regions
858 (0.9-1). **b** Heatmaps demonstrating enrichment patterns of ATAC, 5hmC, and histone modification
859 (H3K4me1, H3K27me3, H3K4me1, and H3K27ac) relative to the center of TET1 peaks (± 5 kb) at
860 proximal (≤ 1 kb from TSS) and distal (> 1 kb from TSS) regions. **c** Venn diagram illustrating distinct
861 and overlapping TET1 binding sites between hESCs and pancreatic progenitors ($p < 0.05$). **d** TF motif
862 enrichment analysis of TET1 targets identified specifically in pancreatic progenitors (top, PP-specific)
863 or hESCs (bottom, ES-specific). The top three motifs are shown. **e** Number of TET1 binding sites
864 identified specifically in pancreatic progenitors (PP-specific) or in both hESCs and pancreatic
865 progenitors (common) at proximal and distal regions ($p < 0.05$). **f** Average plots (top) and heatmaps
866 (bottom) of TET1, H3K4me3, H3K27me3, H3K4me1, H3K27ac, and ATAC at 'common' or 'PP-
867 specific' TET1 peaks (± 5 kb) at proximal or distal regions. Heatmaps are ranked by decreased TET1-
868 binding signal of 'common' and 'PP-specific' regions, respectively. The color scale from white to
869 blue represents the normalized signal from low to high. **g** Distribution profiles of average methylation
870 (5mC), ATAC, H3K4me1, and H3K27ac located at FOXA2-bound sites with (green) or without
871 (orange) co-binding of TET1.

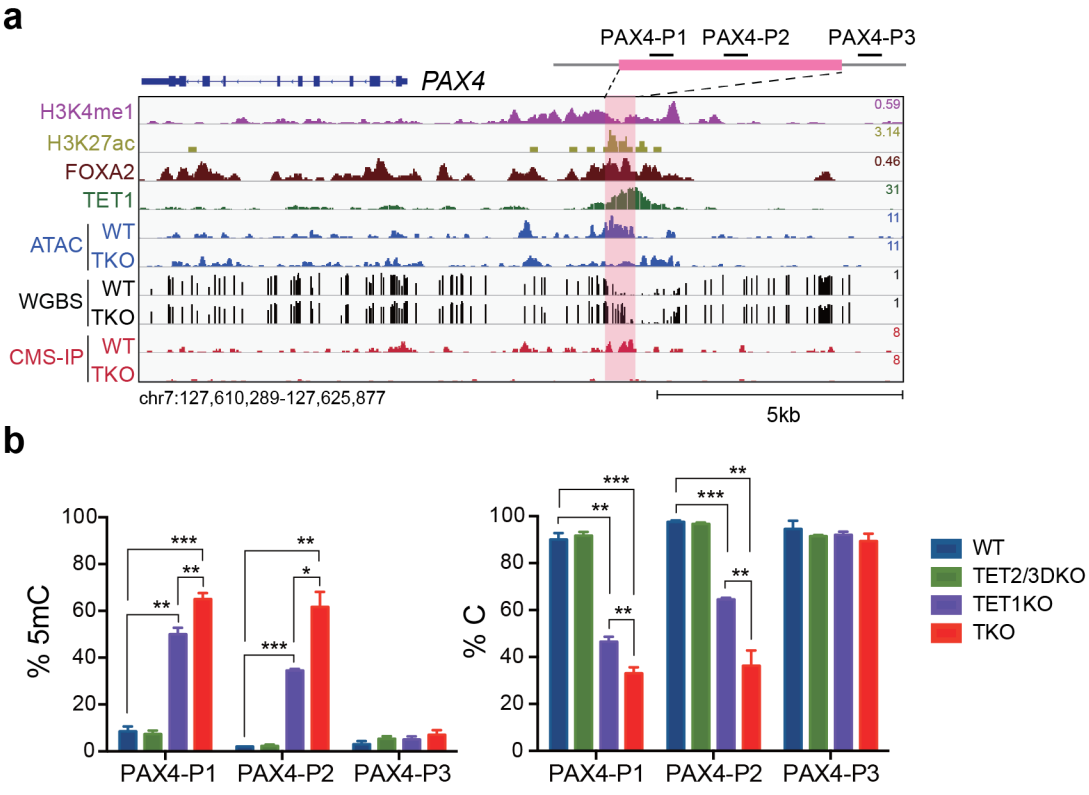

Fig. 6 TET1 is required for the PAX4 enhancer to achieve a hypomethylated state.

a Genome-browser view of the *PAX4* locus with increased methylation and decreased chromatin associability upon TET depletion at a TET1/FOXA2 co-bound region featuring enhancer signatures H3K4me1 and H3K27ac. **b** Locus-specific increase in 5mC at the *PAX4* enhancer in TKO or TET1KO samples compared with TET2/3DKO samples. Percentages of unmethylated cytosine and 5mC at CCGG sites are shown. n = 3 independent differentiation.